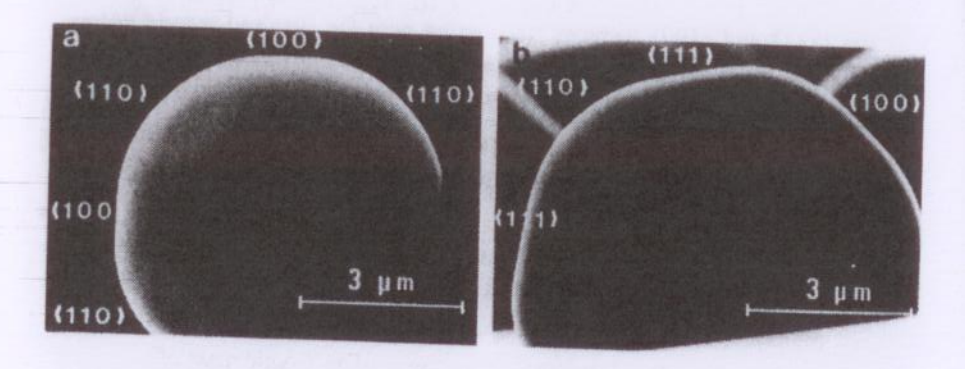


3.8. If a two-dimensional rectangular crystal is bounded by sides of lengths  $l_1$  and  $l_2$ , show by differentiation that the equilibrium shape is given by

$$\frac{l_1}{l_2} = \frac{\gamma_2^{SV}}{\gamma_1^{SV}},$$

where  $\gamma_1^{SV}$  and  $\gamma_2^{SV}$  are the surface energies of sides  $l_1$  and  $l_2$ , respectively. (The area of the crystal  $l_1 l_2$  is constant.)

3.9. The figure below (from [29]) shows two palladium particles on a graphite substrate viewed along (a) <100> and (b) <110>.



- (a) Locate the origin (Wulff point) in both figures.
- (b) Determine the ratio of the surface energy anisotropy for the {100} and {110} surfaces relative to the {111} surface by measuring the lengths of vectors from the origin according to the construction in Figure 3.12.
- (c) Compare the ratio γ<sub>{100}</sub>/γ<sub>{111}</sub> determined in part b with the same ratio determined by comparing the lengths of the {100} and {111} facets, and by comparing the angular width of these facets with respect to the origin. How do your measurements compare?

# SURFACE STRUCTURE

#### 4.1. TERRACE-LEDGE-KINK MODEL OF SURFACES

It is useful to be able to visualize the atomic structures of surfaces and interfaces, because many important phenomena such as the mechanisms and kinetics of crystal nucleation and growth, adsorption and segregation to surfaces and even the definition of the surface depend directly on the atomic structure and atomic level defects present at these interfaces. In this section, we develop an atomic description of crystal surfaces, which we use to further understand the reason for cusps at certain crystallographic orientations in the Wulff plot and to quantify phenomena such as surface roughening (shown schematically in Figure 3.3, but only discussed in a qualitative way). Again, it is important to remember that we are concerned with solid—vapor interfaces (surfaces) in this chapter, but the ideas developed for the terrace-ledge-kink model here are equally applicable to solid—liquid and solid—solid interfaces as we shall see later.

When we considered the formation of an  $\{hkl\}$  surface using the broken-bond model in Chapter 3, we imagined that we created the surface by removing all of the atoms whose centers lay on one side of a mathematical dividing plane with this orientation located within the crystal. Since no atomic relaxations or rearrangements were allowed to occur, the surface was ideal and there was no surface stress. This led to atomic surfaces such as those shown in Figure 3.7. (An atlas of such surfaces for f.c.c. and b.c.c. crystals has been published by Nicholas [18]. This is a useful reference for visualizing various  $\{hkl\}$  surfaces.) The  $\{100\}$  and  $\{111\}$  surfaces shown in Figure 3.7a are atomically smooth and are referred to as singular, because singularities or cusps often occur in the  $\gamma^{SV}$  plot at these orientations.

A surface that is only slightly different in orientation from one that is atomically smooth consists mainly of flat regions called terraces with a system of widely spaced atomic steps or ledges. Such a surface is called vicinal. Figure 4.1a shows a vicinal surface on an f.c.c. crystal that makes an angle of approximately 11° with re-

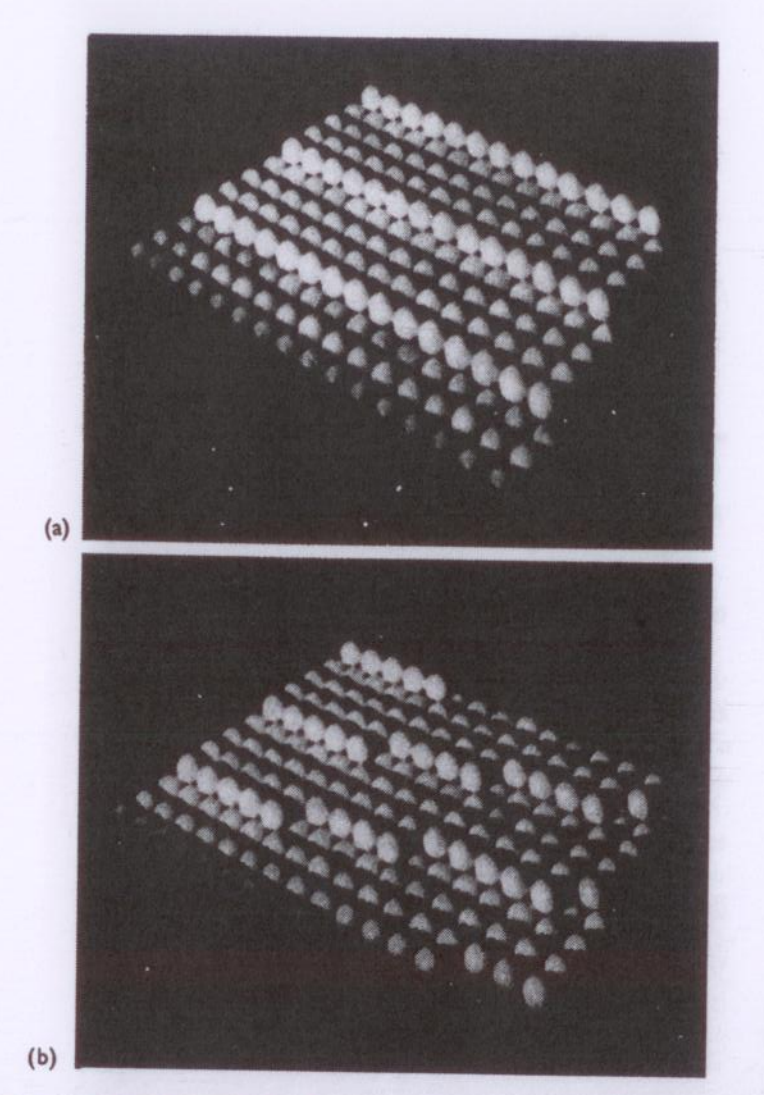


Figure 4.1. (a) An ideal surface of an f.c.c. crystal vicinal to the (100) plane showing straight monotonic steps or ledges. (b) An ideal vicinal surface to (100) with kinks in the ledges. From [6].

spect to the (100) plane and where the ledges are atomically straight because the axis of rotation is parallel to the close-packed [011] ledge direction [6]. In general, the steps on a vicinal surface are not entirely straight, because the axis of rotation is at some angle to the close-packed [011] direction and kinks must be present in the ledges to accommodate the additional tilt, as shown in Figure 4.1b. The surface shown in Figure 4.1b is known as a terrace-ledge-kink (TLK) model of a surface.

For a monotonic solid, the kink site on a vicinal surface is particularly important, because the removal of an atom from such a site to infinity regenerates another kink site but otherwise leaves the crystal unaltered. The work required for such a process thus corresponds to the binding energy per atom of the crystal. We shall make use of this property of the kink site when discussing surface defects shortly. Kinks are often preferred sites of adsorption of impurities to surfaces.

It is possible to construct a theory to predict the shape of  $\gamma^{SV}$  plot cusps on the basis of the terrace-ledge model of vicinal surfaces shown in Figure 4.1a. If the average orientation of the surface deviates from a low-index plane such as {100} or  $\{111\}$  by a small angle  $\theta$ , an array of monatomic ledges of height  $h_1$  and spacing  $\lambda_1$ is created to accommodate the orientation as depicted in Figure 4.1a and illustrated schematically in Figure 4.2. For well-separated ledges, the enthalpy of the surface increases proportionally with the density of the ledges and each ledge also increases the entropy of the surface. The increase in enthalpy and entropy combine to produce an increase in the surface energy that is proportional to  $\theta$ . These effects can be rationalized by noting that atoms along a ledge have fewer nearest neighbors (i.e., more broken-bonds) than those on the terraces and thus a higher enthalpy. This is similar to the behavior of the surface energies in Eqs. 3.18. For example, on the (100) surface shown in Figure 4.1a, the ledge atoms have five broken bonds as compared to the terrace atoms, which have four broken bonds. Thus, to first approximation, we might expect that the excess enthalpy associated with a ledge atom is about  $\frac{1}{4}\gamma^{SV}$ (expressed as energy per atom). The entropy may also increase, because the ledge atoms are less constrained and can vibrate more freely than the terrace atoms and because at finite temperatures, they may also contain kinks that increase the configurational entropy along the ledge.

Using this description for an array of noninteracting monatomic ledges of height  $h_1$  with an excess energy per unit length of ledge  $E_1$ , the surface energy may be written as a function of orientation including both enthalpy and entropy contributions as

$$\gamma^{\text{SV}} = \gamma_0^{\text{SV}} \cos \theta + \left(\frac{\eta E_1}{h_1}\right) \sin \theta,$$
 (4.1)

where  $\gamma_0^{SV}$  is the surface energy of the singular surface and  $\eta$  is a phenomenological parameter that quantifies the entropy of the ledge. This expression is sometimes referred to as the Gruber–Mullins theory [31]. The cos  $\theta$  term accounts for

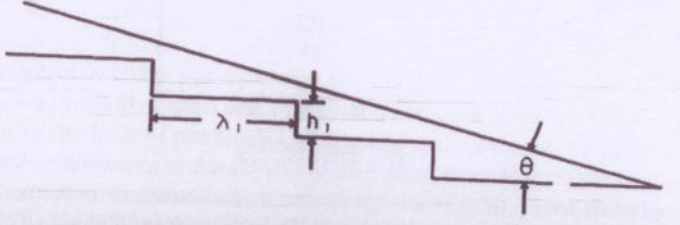


Figure 4.2. Cross section of a vicinal surface showing  $\theta$ ,  $h_l$  and  $\lambda_l$ .

4.2. SURFACE DEFECTS AND SURFACE ROUGHENING

75

the contribution of the terraces or singular surfaces to the surface energy and the  $\sin \theta$  term accounts for the contribution of the ledges to the surface energy. The quantity  $(\sin \theta)/h_1 = 1/\lambda_1$  gives the density of ledges along the surface.

The parameter n is designed to account for both the effects of temperature and interledge spacing on the entropy of the ledge through the quantities  $\beta = \epsilon_b/k_BT$  and θ, respectively. In the limiting case where there is no entropic contribution to the ledges, that is, no tendency for the ledges to wander or kink (0 K for a perfectly straight ledge),  $\eta = 1$  and Eq. (4.1) reduces to a simple form, where  $E_1/h_1$  gives the surface energy  $\gamma_1^{SV}$  of the ledges. As the temperature increases,  $\beta$  decreases and  $\eta$ becomes less than one. Thus, the free energy per unit length of ledge  $E_1$  is reduced by the tendency of the ledge to wander or roughen. Note that the magnitude of this effect is directly related to the interatomic bond strength in the equation for B. The ability of a ledge to roughen also depends on the spacing between the ledges. As  $\theta$ increases and  $\lambda_1$  decreases, the ledges must become straight to avoid interaction. Therefore  $\eta$  increases with  $\theta$  until a critical value is reached  $\theta_{cs}$  where the ledges become straight and  $\eta = 1$ . Figure 4.3 illustrates the relationship among  $\eta$ ,  $\beta$  and  $\theta$  for a (100)[011] ledge system in an f.c.c. crystal like the one shown in Figure 4.1a. Note that as  $T \to 0$  K,  $\beta \to \infty$  and  $\eta \to 1$  in Figure 4.3, and the ledge entropy contribution vanishes. As the temperature increases above 0 K, the parameter B de-

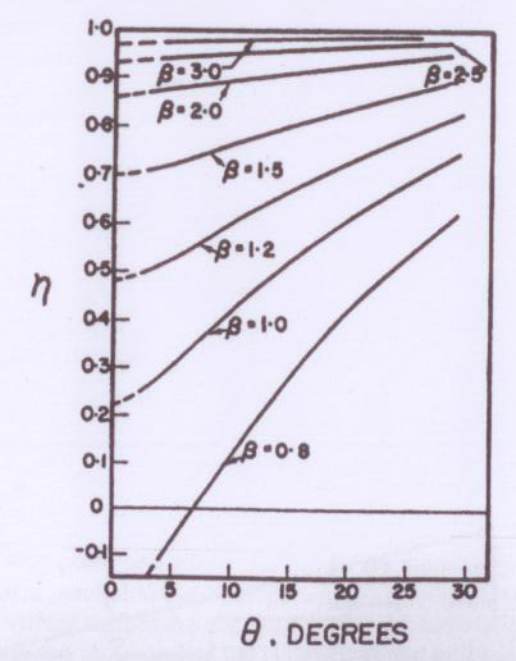


Figure 4.3.  $\eta$  versus  $\theta$  for a  $(100)[01\overline{1}]$  ledge system for various values of the parameter  $\beta$ , where  $\theta_c$  = 54.74°. Reprinted with permission from [31] by Elsevier Science Ltd., Oxford, England.

creases for a given angle due to roughening of the ledge from thermal kinks. As  $\theta$  increases,  $\eta$  increases because the ledges must straighten to avoid interaction (i.e., overlapping one another).

The main result of Eq. (4.1) is that a plot of  $\gamma^{\rm SV}$  versus  $\theta$  has a cusp when  $\theta$  equals zero and the magnitude of this cusp is proportional to the free energy increase for each ledge added  $(\eta E_l/h_l)$ . In addition, the magnitude of  $\gamma^{\rm SV}$  decreases with increasing temperature, because  $\eta$  is a decreasing function of temperature. These characteristics are qualitatively displayed by the graphs for lead in Figure 3.16. It is important to note that there is a strong similarity between the model behind Eq. (4.1) and the dislocation model of a low-angle grain boundary (Chapter 13); in both cases, the atomic disorder is localized at line defects that correspond to the termination of planes of atoms at the interface.

If we differentiate Eq. (4.1) with respect to T and  $\theta$ , and assume that  $\partial \gamma^{\rm SV}/\partial \theta$  becomes negligibly small as  $\theta$  tends to zero, it is possible to determine the following relationships for the various enthalpic and entropic parameters:

$$\gamma_{(\theta \to 0)}^{SV} = \gamma_0^{SV} \quad \text{and} \quad S_{(\theta \to 0)} = S_0;$$
(4.2)

$$\frac{\partial \gamma_{(\theta \to 0)}^{SV}}{\partial \theta} = \frac{E_1}{h_1} \quad \text{and} \quad \frac{\partial S_{(\theta \to 0)}}{\partial \theta} = -\frac{\partial E_1/\partial T}{h_1}, \tag{4.3}$$

where  $(-\partial E_1/\partial T)$  is the ledge entropy. Estimates of these parameters can be made by measuring the intercepts and gradients of the  $\gamma^{\rm SV}$  plots  $(\partial \gamma^{\rm SV}/\partial \theta)$  and entropy plots  $(\partial S/\partial \theta)$  around low-index poles. Comparison between experiment and this theory has met with varying degrees of success. One favorable case is shown for vicinal surfaces of copper near {100} in Figure 4.4 [24]. Table 4.1 also shows values of the surface energy, surface entropy, ledge enthalpy and ledge entropy obtained for {100} copper as a function of temperature in this investigation, using Eqs. (4.2) and (4.3).

# 4.2. SURFACE DEFECTS AND SURFACE ROUGHENING

So far, we have considered the structure of a crystal surface as ideal and free from any relaxations or defects, except for the possible presence of ledges and kinks when the surface is vicinal. In this and the following sections, we examine a variety of interesting defects and behavior associated with real crystal surfaces.

Defects in a surface can generally be divided into two categories, those that are thermodynamically stable and those that are kinetically stable. The kinetically stable class includes primarily points of dislocation emergence at the surface. Dislocations are present in the bulk of practically all crystals and they must be present either as closed loops or networks in the crystal or they must terminate on the crystal surface [32]. Thermodynamic point defects are stable above 0 K. These defects all have a positive free energy of formation from the structure given by the TLK model, but they are stable in finite quantities because of the favorable change in entropy associ-

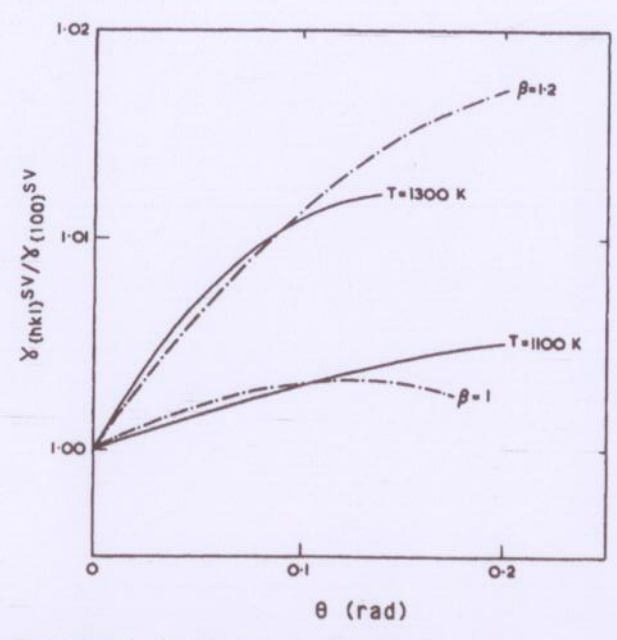


Figure 4.4. Comparison of experimental data (solid curves) for copper with the Gruber-Mullins theory (dashed curves) close to {100}. Reprinted with permission from [24] by Elsevier Science Ltd., Oxford, England.

ated with the disorder produced in an initially ideal system. We briefly decribe kinetically stable dislocations and then discuss thermodynamically stable defects.

There are two primary types of dislocations: an edge and a screw dislocation. Schematic illustrations of the termination of edge and screw dislocations with a crystal surface are shown in Figure 4.5. In both cases, the line direction of the dislocation is taken as normal to the crystal surface. The edge dislocation is essentially associated with an extra half-plane of atoms in the bulk of the crystal, indicated by the  $\bot$  in Figure 4.5a. Edge dislocations have different bonding configurations than normal surface atoms and thus behave differently in gas—surface interactions such as adsorption or surface chemical reactions. The emergence of a screw dislocation creates a step on the surface of a crystal, one end of which is tied to the site of dislo-

Table 4.1. Temperature dependence of surface and ledge enthalples and entropies near {111} Cu

Temp. (°C)	Surface Enthalpy (mJ/m²)	Surface Entropy (mJ/m <sup>2.</sup> °C)	Ledge Enthalpy (J/m)	Ledge Entropy (J/m.°C)
827	1448	0.33	1.8×10 <sup>-11</sup>	0.7×10 <sup>-13</sup>
927	1415	same	1.2×10-11	same
1027	1382	same	0.5×10 <sup>-11</sup>	same

Source: From [24].

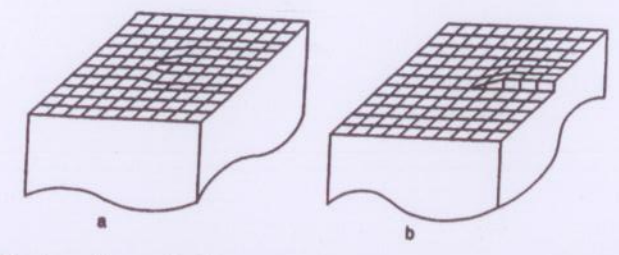


Figure 4.5. Simple cubic models illustrating the sites of emergence of (a) edge and (b) screw dislocations onto the crystal surface. From [33],

cation emergence as shown in Figure 4.5b. As we shall see in subsequent sections, the presence of such steps has a large influence on the growth of crystals from the vapor or solution. Because the step is tied to the site of dislocation emergence, it has the property of being continuously regenerated as crystal growth proceeds, thus eliminating the nucleation barrier to growth. A transmission electron microscope (TEM) image of screw dislocation spirals on the surface of a sodium chloride crystal revealed by the gold decoration technique is shown in Figure 4.6 [34].



Figure 4.6. Growth step patterns on a sodium chloride cleavage surface revealed by the gold decoration technique (evaporation and preferential adsorption of gold atoms to the ledges on the surface) in a transmission electron microscope. From [10,34] reprinted with the permission of Cambridge University Press.

79

We now turn our attention to thermodynamically stable defects. In addition to the terraces, ledges and kinks that were described previously, a variety of other types of defects can be present on crystal surfaces. Figure 4.7 shows some of the more common possibilities using a simple cubic {100} surface for ease of illustration. On an f.c.c. {111} surface such as that in Figure 3.7a, the number of nearest neighbors adjoining a surface (terrace) atom is 9, adjoining a ledge atom is 7, adjoining a kink atom is 6, adjoining a ledge adatom is 5, and adjoining a surface (terrace) adatom is 3. The reader is encouraged to derive these numbers for an f.c.c. {111} surface using a hard sphere model, such as Figure 4.1.

The surface defects shown in Figure 4.7 are present at equilibrium at any temperature above 0 K for thermodynamic reasons and are similar in concept to the vacancies and interstitial atoms found at equilibrium in bulk crystals [35]. To illustrate the importance of these defects in real crystal surfaces, we look at the phenomenon of surface roughening from two different viewpoints. First, we use a nearest-neighbor bond model and simple analytical expressions to examine the roughness of low-index terraces and ledges as a function of temperature. Second, we compare our simple calculational results with those from more sophisticated computer calculations. As in our treatment of surface anisotropy, we see that the simple nearest-neighbor bond model yields qualitatively, although not quantitatively, correct results for surface roughening.

#### 4.2.1. Analytical Treatment of Terrace and Ledge Roughening

The phenomenon of surface roughening was initially treated in the classic work by Burton, Cabrera and Frank [36], as was the TLK model of surfaces in the previous section, but here we follow a somewhat simpler treatment developed by Mullins [37] and Hirth [27] that yields the same result. In our analytical treatment, we consider {111} and {100} f.c.c. crystal surfaces using a three-level, nearest-neighbor bond model, which includes surface atoms, surface adatoms and surface vacancies. Because the addition or removal of an atom from a kink regenerates another identi-

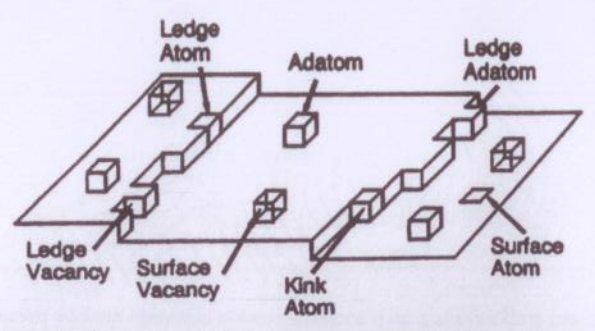


Figure 4.7. Schematic view of a vicinal surface showing low-index terraces, monatomic ledges, atoms and vacancies at various positions on the terraces and ledges. From [27,33].

cal kink but otherwise leaves the crystal unaltered, we assume that equilibrium among these defects is obtained through kinks in ledges.

Consider a unit area of a  $\{111\}$  surface of an f.c.c. crystal in which the atoms are bounded by nearest neighbors with bond energy  $\epsilon_b$ . The surface is infinite in extent except for the presence of one ledge containing one kink. To create a vacancy, we remove a surface atom, breaking nine bonds, and replace it at a kink site, restoring six bonds. Thus, the net energy of forming a vacancy is  $3\epsilon_b$ . (The same procedure can be used to calculate the energy of formation of the other defects in Figure 4.7.) If we now create  $n_v$  vacancies per unit area of surface, the energy of vacancy formation is

$$E_{v} = 3\epsilon_{b}n_{v} - \frac{6\epsilon_{b}n_{v}^{2}}{N_{s\{111\}}},$$
(4.4)

where the second term arises as a correction for surface divacancies, and  $N_{s\{111\}}$  is the number of surface sites per unit area on the  $\{111\}$  surface. If there is no binding energy between vacancies, then the number of divacancies is  $n_v$  times  $6n_v/N_{s\{111\}}$ , that is, the probability that an adjacent site is also vacant times ½, because, in such a procedure, each divacancy is counted twice. The energy contribution from divacancies is equal to this number times 4, the difference between the free half-bonds of two single vacancies and a divacancy, times the half-bond energy  $\epsilon_b/2$ . In the remainder of this treatment, we assume that there is no binding between divacancies.

If we assume that an adatom cannot occupy a site overhanging a vacancy, the number of ways of distributing  $n_v$  vacancies among  $N_s = (N_{s\{111\}} - 3n_a)$  sites, where  $n_a$  is the number of adatoms, each of which excludes three sites, is

$$\xi = \exp \frac{S}{k_{\rm B}} = \frac{N_{\rm s}!}{(N_{\rm s} - n_{\rm v})! n_{\rm v}!},$$
(4.5)

based on standard Fermi-Dirac statistics [38]. Applying Stirling's approximation [38], the Helmholtz free energy of formation of  $n_v$  vacancies is

$$F = E - TS = 3\epsilon_{b}n_{v} - \frac{6\epsilon_{b}n_{v}^{2}}{N_{s\{111\}}}$$

$$-k_{B}T[N_{s} \ln N_{s} - (N_{s} - n_{v}) \ln (N_{s} - n_{v}) - n_{v} \ln n_{v}].$$
(4.6)

We can then obtain the equilibrium concentration of vacancies from the condition that  $(\partial F/\partial n_{\nu}) = 0$ , yielding

$$\frac{n_{\rm v}}{N_{\rm s\{111\}} - 3n_{\rm s} - n_{\rm v}} = \exp\left[-\left\{\frac{3\epsilon_{\rm b}}{k_{\rm B}T}\left[1 - 4(n_{\rm v}/N_{\rm s\{111\}})\right]\right\}. \tag{4.7}$$

In the case of adatoms, there are two possibilities. First, if adatoms are constrained to occupy only the normal f.c.c. sites, then the derivation of  $n_a$  follows the above treatment for  $n_v$  exactly and an equation like Eq. (4.7) results, with  $n_a$  and  $n_v$  simply

4.2. SURFACE DEFECTS AND SURFACE ROUGHENING

interchanged. If, on the other hand, both normal f.c.c. sites and sites corresponding to h.c.p. sites, both of which have three nearest neighbors to an adatom are occupied, then twice as many sites are available to adatoms, but each vacant site excludes six adatom sites and each adatom excludes three adatom sites. Thus the adatom equivalent of Eq. (4.7) in this case becomes

$$\frac{n_{\rm a}}{2N_{\rm s\{111\}} - 6n_{\rm v} - 4n_{\rm a}} = \exp\left[-\frac{3\epsilon_{\rm b}}{k_{\rm B}T}\left[1 - 4(n_{\rm a}/N_{\rm s\{111\}})\right]\right]. \tag{4.8}$$

For a {100} surface of an f.c.c. crystal (or a simple cubic crystal), we can similarly obtain the expressions

$$\frac{n_{\rm v}}{N_{\rm s\{100\}} - n_{\rm v} - n_{\rm a}} = \exp\left[-\left\{\frac{2\epsilon_{\rm b}}{k_{\rm B}T}\left[1 - 2(n_{\rm v}/N_{\rm s\{100\}})\right]\right\}$$
(4.9a)

$$\frac{n_{\rm a}}{N_{\rm s\{100\}} - n_{\rm v} - n_{\rm a}} = \exp\left[-\frac{2\epsilon_{\rm b}}{k_{\rm B}T} \left[1 - 4(n_{\rm s}/N_{\rm s\{100\}})\right]\right]. \tag{4.9b}$$

Noting, in this case, that  $n_a = n_v$  and letting  $X = X_v = X_a$ , where  $X_v$  is the mole fraction of vacancies and  $X_a$  is that of adatoms, Eqs. 4.9a and b both become

$$\frac{X}{1-2X} = \exp\left[\frac{2\epsilon_{\rm b}}{k_{\rm B}T}(1-2X)\right]. \tag{4.10}$$

Following Burton et al. [36], we can define the surface roughness s as the number per site of free bonds parallel to the surface, which in the case of  $\{100\}$  gives

$$s = \frac{E_{\rm v}}{N_{\rm s}(\epsilon_{\rm b}/2)} = 8X(1 - X). \tag{4.11}$$

A plot of s versus  $(k_BT/\epsilon_b)$  obtained by simultaneous solution of Eqs. (4.10) and (4.11) is shown by the solid line in Figure 4.8. The dashed line corresponds to the treatment of Burton et al. [36]. Note that the quantity  $(k_BT/\epsilon_b)$  in Figure 4.8 is the inverse of the term  $\beta$  used in the previous section in the Gruber-Mullins analysis. Because  $\epsilon_b$  is the nearest-neighbor bond energy, the quantity  $(k_BT/\epsilon_b)$  is a measure of the amount of (thermal) energy present in the system relative to the nearest-neighbor bond energy of the atoms. [The bond energy can be obtained by noting that  $\Delta H_s$ , the heat of sublimation, equals the energy needed to remove an atom from a kink site to the vapor. For an f.c.c. crystal this energy is  $6\epsilon_b$ , so that  $\epsilon_b = \Delta H_s/6$  (J/mol) as defined in Eq. (1.4).] The results in Figure 4.8 predict that s is appreciable only for  $(k_BT/\epsilon_b) > 0.5$ . If  $\epsilon_b$  is on the order of 337 kJ/mol, as for copper in Table 1.1, then Figure 4.8 predicts that roughening of the surface would occur only at temperatures an order of magnitude higher than the melting point of copper. Thus, we can conclude from Figure 4.8 that low-index planes should not become rough below the melting point. Experimentally, this is known not to be true; surfaces can display

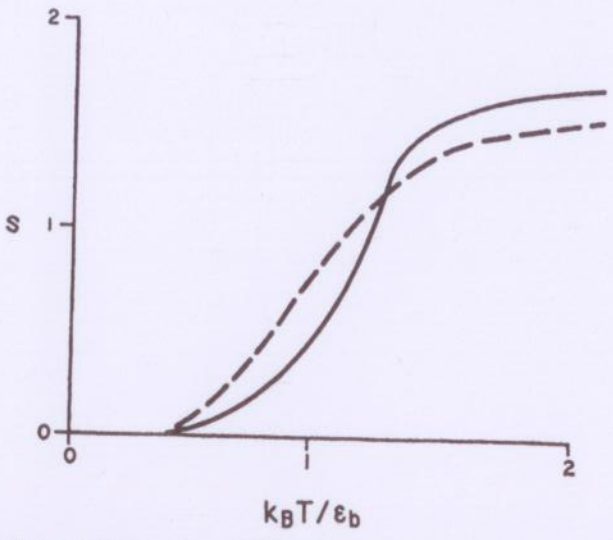


Figure 4.8. Surface roughness s for a {100} surface of an f.c.c. (or simple cubic) crystal as a function of  $(k_BT/\epsilon_b)$ . From [27].

considerable roughness at temperatures well below the melting point. For example, Figure 4.9 shows a scanning-tunneling-microscope (STM) image of a surface vicinal to {100} silicon, where the distance between the ledges is approximately 17 nm. A variety of defects including vacancies and adatoms on both the terraces and ledges are clearly visible in the figure. Similar results have been obtained for other materials, indicating that, although the behavior of the surface roughness is qualitatively described by the curves in Figure 4.8 (i.e., the surface continually roughens with temperature until it is no longer well defined), the nearest-neighbor bond model cannot be used to determine the actual temperature dependence for a particular material.

To fully describe the behavior of a TLK model of a surface with respect to temperature, we need to consider roughening of ledges in addition to roughening of the terraces. If we take the case of a <110> ledge on an  $\{111\}$  f.c.c. surface, the energy of formation of  $n_v^1$  ledge vacancies is

$$\epsilon_{\rm b} n_{\rm v}^{\, 1} - [\epsilon_{\rm b} (n_{\rm v}^{\, 1})^2 / N_{\rm l}],$$
 (4.12)

where  $N_1$  is the number of available ledge sites. Continuing as in the previous treatment of terraces, we obtain

$$\frac{n_{\rm v}^{\rm I}}{N_{\rm l} - n_{\rm v}^{\rm I} - n_{\rm a}^{\rm I}} = \exp\left[\frac{\epsilon_{\rm b}}{k_{\rm B}T} (1 - 2X_{\rm v}^{\rm I})\right]$$
(4.13a)

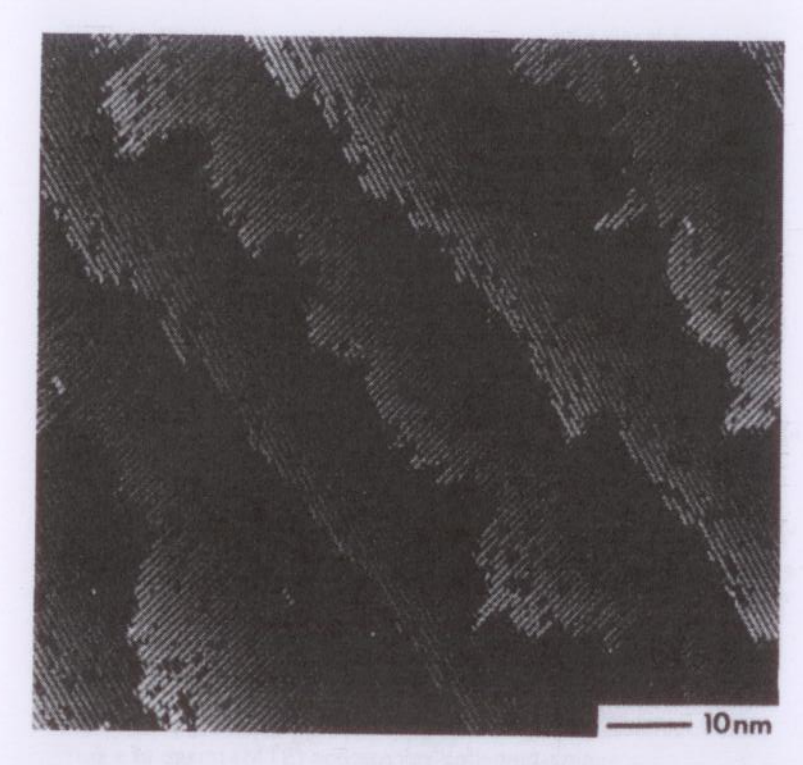


Figure 4.9. STM image of a vicinal silicon (100) ( $2 \times 1$ ) reconstructed surface. The white lines are dimer rows on the surface. The nomenclature used to describe the reconstruction and the dimer rows are described in subsequent sections. From [10,39] reprinted with the permission of Cambridge University Press.

$$\frac{n_{\rm a}^{\rm l}}{N_{\rm l} - n_{\rm a}^{\rm l} - n_{\rm v}^{\rm l}} = \exp\left[-\frac{\epsilon_{\rm b}}{k_{\rm B}T}(1 - 2X_{\rm a}^{\rm l})\right]. \tag{4.13b}$$

In this case, the energy of formation of defects is much less than in the case of the low-index surface, and roughening typically becomes appreciable at temperatures of approximately one-half the melting point of a material. In fact, above such a temperature, it becomes more meaningful to consider the kink concentration rather than the concentration of ledge vacancies and adatoms. Note that a single ledge vacancy, a divacancy, and so on, are all equivalent to two kinks of opposite sign displacement. Burton et al. [36] considered the statistical thermodynamical problem of kink formation and, for the above example of a  $\{111\}$  f.c.c. surface, found that  $n_k$ , the number of kinks per unit length of ledge, is given by

$$\frac{n_{\rm k}}{N_{\rm l}} = \exp\frac{-E_{\rm k}}{k_{\rm B}T} = \exp\frac{-\epsilon_{\rm b}}{2k_{\rm B}T},\tag{4.14}$$

where  $E_k$  is the energy of formation of a kink (half the energy of formation of a va-

cancy because a vacancy is equivalent to two kinks). Equation (4.14) is quite useful, because it can be used to determine the ledge energy and kink formation energies by counting the number of kinks per unit length along ledges in STM images, such as those in Figure 4.9, as a function of the temperature at which the surface was equilibrated before the STM measurements. These measurements have been performed for the {100} silicon surface and the ledges that run parallel to the dimer rows have an energy of 0.028 eV/atom, whereas those that run perpendicular to the dimer rows have an energy of 0.09 eV/atom. An excess energy of 0.08 eV is associated with each kink site. Note that the ledges that run parallel to the dimer rows in Figure 4.9 are less kinked, because their excess energy is lower and they are more stable.

The picture that emerges from our analytical nearest-neighbor bonding treatment of ledges is that they become appreciably rough at a temperature of about  $0.5T_{\rm m}$ . This agrees conceptually with the inclusion of ledge roughness as a function of temperature in the phenomenological parameter  $\eta$  in Figure 4.3 and with a number of experimental results. As we shall see below, it also agrees with the picture that emerges from more sophisticated computer calculations.

# 4.2.2. Computer Calculation of the Equilibrium Structure of Crystal Surfaces

The equilibrium structures of <100> oriented steps on vicinal {100} surfaces have been examined by Monte Carlo methods [40]. The purpose of the work was to determine the energy of isolated ledges and the thermodynamic properties of surfaces with different ledge densities. Thus {100}, (21 1 0}, {10 1 0} and {510} surfaces of a simple cubic crystal were studied as a function of  $k_B T/\epsilon_b$ , assuming nearest-neighbor interactions of strength  $\epsilon_b = \Delta H_s/3$ . By determining the ledge density dependence of the surface energy as a function of temperature and orientation [just as in Eqs. (4.1) and (4.3) and Problem 4.2], it was possible to extract the temperature dependence of an isolated <100> ledge. The energy of the ledge  $E_1$  is shown as a function of temperature in Figure 4.10. The energy of the ledge first rises with temperature as a result of thermal excitation until, in a critical region,  $E_1$  decreases rapidly to zero at the roughening temperature  $T_F$ .

Figure 4.11 shows computer drawings of the stable structures generated during simulation of the  $\{21\ 1\ 0\}$  surface at several values of  $k_BT/\epsilon_b$ . At the lowest temperature illustrated, where  $k_BT/\epsilon_b=0.428$ , the ledge is noticeably rough, but no excitations appear greater than unit height perpendicular to the surface. As the temperature is increased into the critical region, the incidence of greater-than-unit-height excitations near the step edges increases until  $E_1=0$ , and they are no longer distinguishable. This arises because thermal roughening of the terraces effectively camouflages the ledges introduced into the simulation by the boundary conditions. This dramatic change in surface topography is associated with the surface roughening transition indicated in Figure 4.10. Unlike the two-dimensional Ising model indicated in Figure 4.10 and the previous analytical treatment where the height of the roughened surface was confined to only one atomic dimension above or below the surface plane (i.e., a three-level model containing only single adatoms and vacan-

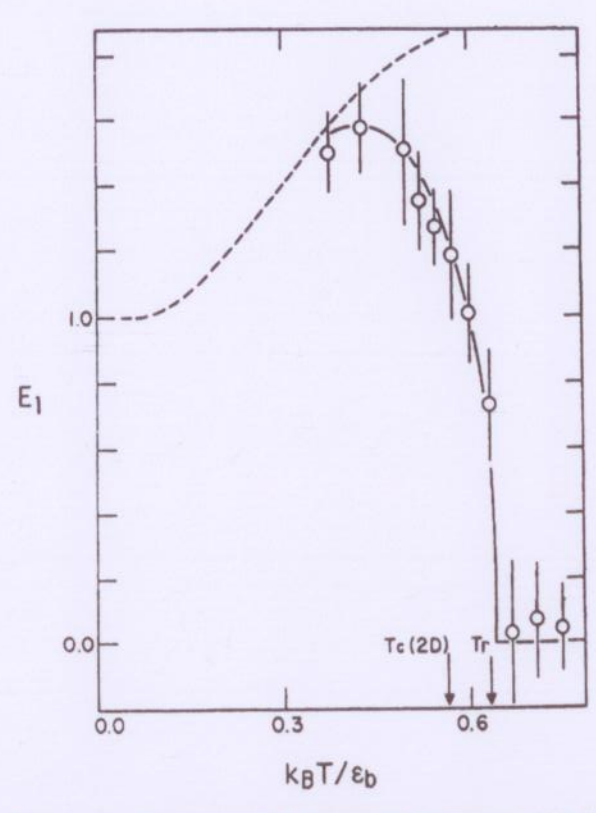


Figure 4.10. Temperature dependence of the energy of an isolated <100> ledge on the  $\{100\}$  surface of a simple cubic crystal. The dashed line represents the energy of an interface in a two-dimensional Ising model. Vertical arrows indicate the two-dimensional Ising model critical temperature  $T_c$  and the roughening transition temperature  $T_c$ . Reprinted from [40] with kind permission from Elsevier Science-NL, Amsterdam, The Netherlands.

cies), Figure 4.11 shows that higher excitations occur above  $T_c$ . This change in the nature of the excitations is manifested by a smooth decrease of  $E_1$  to zero at  $k_BT/\epsilon_b \sim 0.64$ . The data in Figure 4.10 were fitted to an equation of the form

$$E_{\rm I} \propto [(T_{\rm r} - T)/T_{\rm r}]^{0.38},$$
 (4.15)

where 0.64 was used as  $k_BT_i/\epsilon_b$ . This simulation combines the effects of both terrace and ledge roughening to provide an atomistic description that explains the behavior of surfaces with temperature. Note that it agrees qualitatively with most of the results from the previous descriptions of ledges and terraces. It also predicts that at the roughening transition, the cusp in the Wulff plot for a low-index surface vanishes. (Note that this is a second-order transition with a general behavior similar to the loss of long-range order shown in Figure 2.12.)

The effect of surface roughening on the equilibrium crystal shape is illustrated

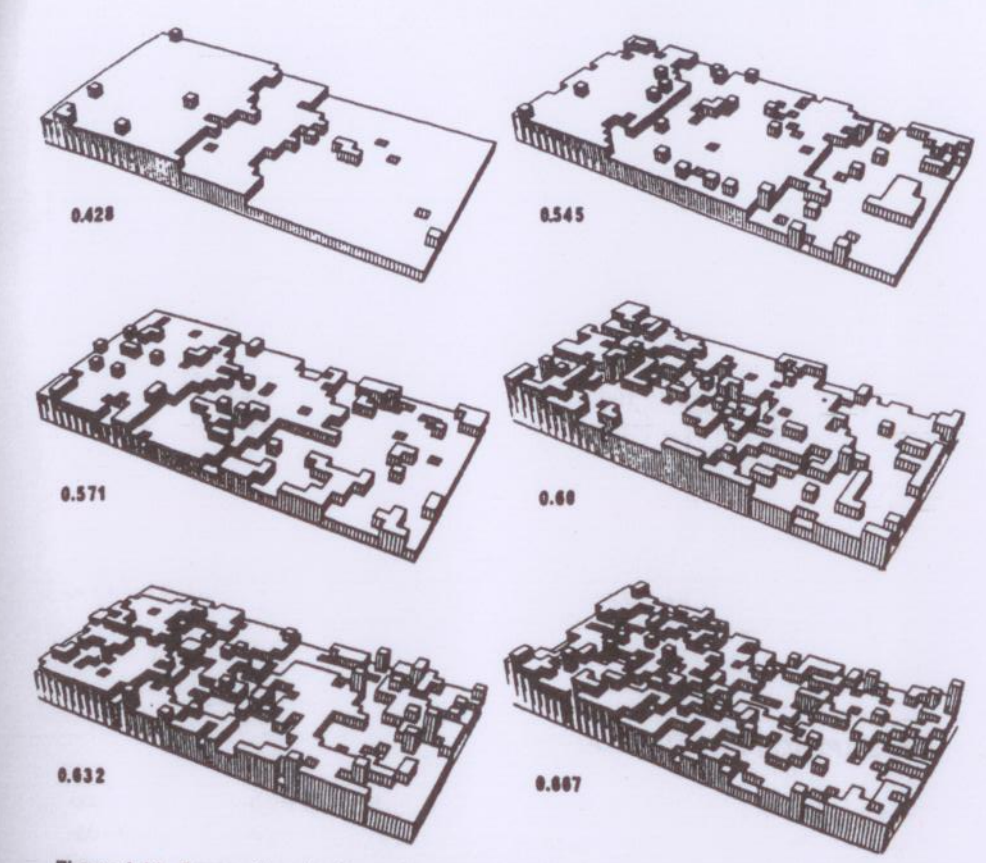


Figure 4.11. Perspective drawings of representative  $\{21\ 1\ 0\}$  surface configurations at various values of  $k_{\rm B}T/\epsilon_{\rm b}$ . Reprinted from [40] with kind permission from Elsevier Science-NL, Amsterdam, The Netherlands.

schematically in Figure 4.12. At T=0, the equilibrium crystal shape for a typical nearest-neighbor simple cubic crystal is a square, as illustrated in Figure 4.12a. As the temperature is increased but is still below  $T_r$  for the  $\{100\}$  surface, the  $\{100\}$  facets remain but are now separated by smoothly curved surfaces due to roughening of the sharp corners. An example of this state is displayed by the lead crystals in Figure 3.15. As the temperature approaches the  $\{100\}$  roughening transition temperature, the facets shrink to zero, and above  $T_r$  the equilibrium crystal shape is a single smoothly rounded surface without edges. As we might expect from our treatment of surface anisotropy, the value of the roughening temperature varies with surface orientation, generally being higher for low-index surfaces that display deep cusps in the Wulff plot. This leads to the concept of a surface-roughening phase diagram, as illustrated for the simple cubic crystal in Figure 4.12b. Note that  $T_r$  is highest for the vicinal  $\{100\}$  surfaces and that the  $\{110\}$  surface at 45° is rough at 0 K, because, in this simple cubic model, it is composed of atom-high ledges spaced one atom apart.

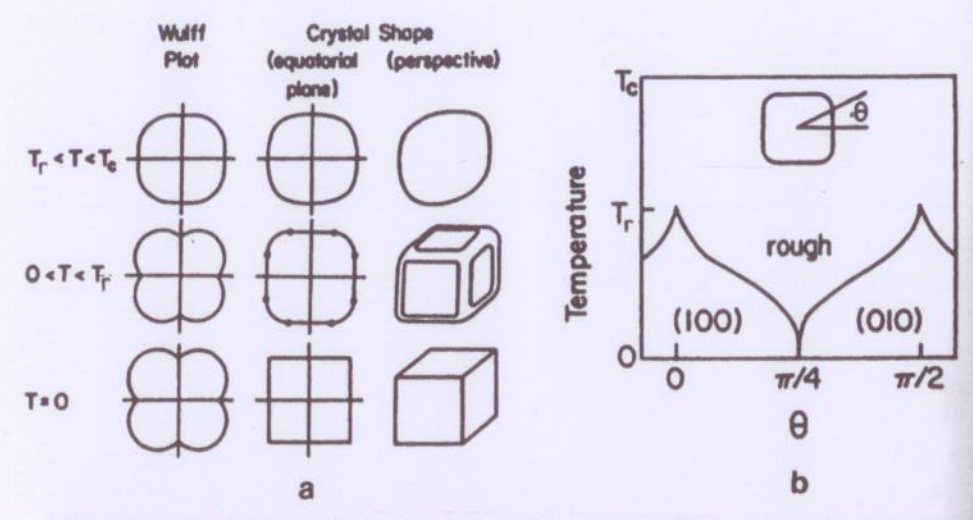


Figure 4.12. (a) Equilibrium shape of nearest-neighbor simple cubic crystal as a function of temperature T. The evolution of the edge position in the equitorial plane is shown in the phase diagram in (b), where  $T_r$  is the roughening temperature of the {100} surface and  $\theta$  is the angle of the surface normal from (100). From [41].

#### 4.3. SURFACE CRYSTALLOGRAPHY

We would like to continue our discussion of real surfaces to include surface relaxations and reconstructions. To do this, we need first to discuss the notation conventionally used to describe the structure of crystal surfaces. We already have encountered an example of this notation with regard to the silicon (100) (2 × 1) surface shown in Figure 4.9; here we develop this notation further.

Surface structures are usually described in terms of their relationship with the underlying bulk structure. The substrate lattice parallel to the surface is taken as the reference net and the surface net is indexed with respect to the substrate. Any translation between lattice points on the substrate net can be described by a translation vector

$$T = na + mb$$
  $(n, m = 0, 1, 2...),$  (4.16)

where a and b are vectors that define the unit cell of the two-dimensional lattice. There are only five lattice types in two dimensions, commonly called the five twodimensional Bravais lattices. Similarly, for translations between lattice points on the surface net, we have

$$T_s = n'a + m'b \quad (n', m' = 0, 1, 2...).$$
 (4.17)

In many cases, the relationship between T and T, is such that

$$a_s = pa$$
 and  $b_s = qb$   $(p,q = 0, 1, 2...)$  (4.18)

and the surface unit-cell vectors are parallel to those of the substrate. The five twodimensional surface nets are illustrated in Figure 4.13.

In the case of a clean ideal surface without relaxation, p and q are both unity. The arrangement of surface atoms that is identical to that in the bulk unit cell is called the substrate structure and is designated (1 × 1). For example, the substrate structure of gold on the (111) surface is designated gold (111) (1 × 1). Other arrangements of surface atoms are called surface structures. It is often found that surface structures can be characterized by unit cells that are integral multiples of the substrate unit cell. If the unit cell of the surface structure is twice as large as the underlying bulk unit cell, it is designated (2 × 2). If it is twice as long in one direction but has the same length as the substrate in the other, it is designated (2 × 1). Figure 4.14 shows examples of some frequently occurring surface structures with two-, four- and six-

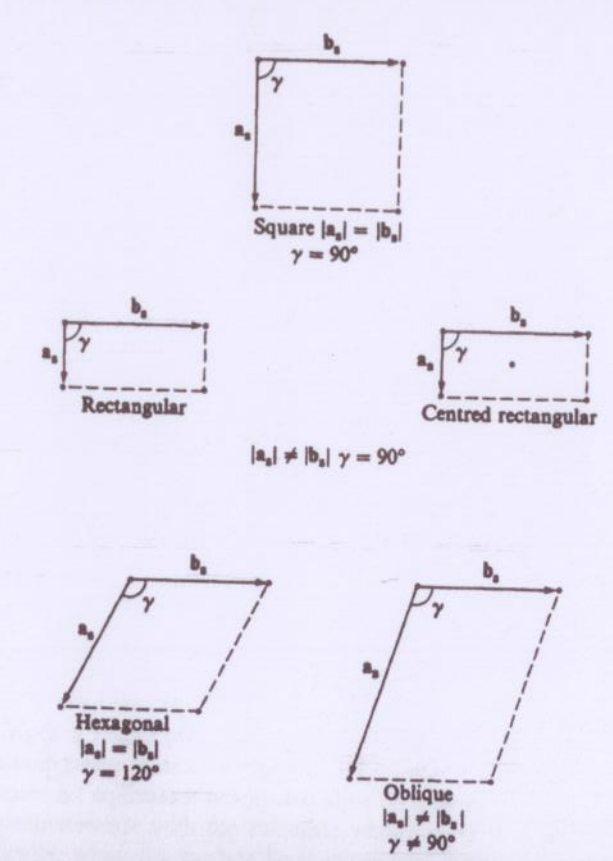
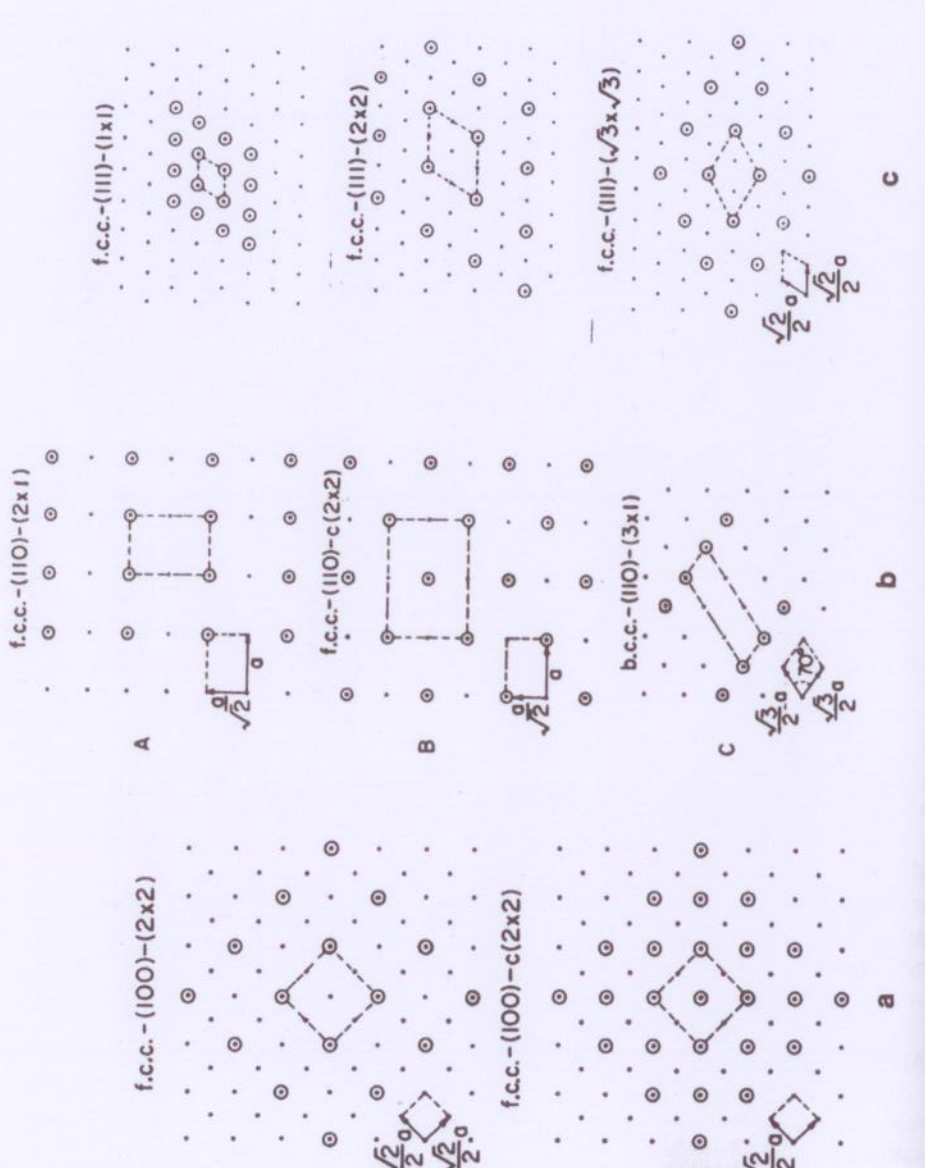


Figure 4.13. The five two-dimensional surface nets with the unit-cell vectors as and bs and included angle y. The centered rectangular net is a special case of the oblique net with nonprimitive lattice vectors (i.e., more than one lattice point per unit cell). From [10] reprinted with the permission of Cambridge University Press.



diagrams of f.c.c. surface structures with (a) two-, (b) four- and (c) sixfold ro-indicate the positions of substrate atoms and the open circles indicate sur-

fold rotational symmetry on f.c.c. substrates. Note that in some cases it is preferable to construct a centered unit cell to avoid noninteger notation for the surface structure. The letter c is added to the notation to indicate a centered unit cell.

In many instances, the surface structure that forms is due to the presence of an adsorbed species on the substrate. In this case, the surface structure is described with respect to the substrate using the same notation as above, but the chemical identities of the substrate and surface atoms must be added. The notation then becomes

$$M(hkl)(p \times q) - B, \tag{4.19}$$

where M is the chemical species of the substrate, (hkl) are the Miller indices of the substrate orientation, p and q are integers that relate the surface structure (unit cell) to the bulk structure, and B is the chemical species of the surface [42]. For example, a surface that was formed by cutting a nickel crystal parallel to the (100) plane of the crystal and adsorbing oxygen on the surface to form a surface structure that had twice the periodicity of the substrate in both the a and b directions would be designated Ni (100) (2 × 2) – O.

In even more complicated cases where the surface and substrate vectors are not parallel to one another, a similar notation is still used and is written as

$$M(hkl) (\mathbf{a}_s/\mathbf{a} \times \mathbf{b}_s/\mathbf{b}) R\alpha - B,$$
 (4.20a)

where

$$\mathbf{a}_{s} = p_{1}\mathbf{a} + q_{1}\mathbf{b}, \quad \mathbf{b}_{s} = p_{2}\mathbf{a} + q_{2}\mathbf{b}$$
 (4.20b)

and R indicates a rotation of the surface structure relative to the bulk structure through an angle  $\alpha$ . For example, a commonly observed structure for a nickel (111) surface with adsorbed oxygen atoms is Ni (111)  $(\sqrt{3} \times \sqrt{3}) R30^{\circ} - 0$ . This type of structure is shown schematically in Figure 4.14c, where the dots indicate nickel atoms and the open circles represent oxygen atoms. If every other lattice site on a nickel (100) surface is covered with oxygen, then a Ni (100)  $(\sqrt{2} \times \sqrt{2}) R45^{\circ} - 0$  surface structure results. To avoid noninteger notation for this structure, it is usually labeled Ni (100)  $c(2 \times 2) - 0$ , as illustrated schematically in Figure 4.14b. In very complicated cases, it becomes necessary to use a matrix notation to completely specify the surface structure [43] but this is not described here.

Because surface layers often involve adsorbed atoms, it is sometimes convenient to define the adsorbate coverage  $\Theta$ , so that  $\Theta = 1$  occurs when an adsorbed species occupies all equivalent adsorption sites on a surface. A surface structure is said to be commensurate with the substrate whenever  $\Theta$  is a rational number, or, more specifically, when the surface layer symmetry differs from that of the substrate by the addition or subtraction of certain symmetry elements. Adsorbed structures whose symmetry is accidentally related to the substrate are called incommensurate. Examples of increasing coverage of nickel (110) by hydrogen and

commensurate/incommensurate structures of krypton on graphite are shown below.

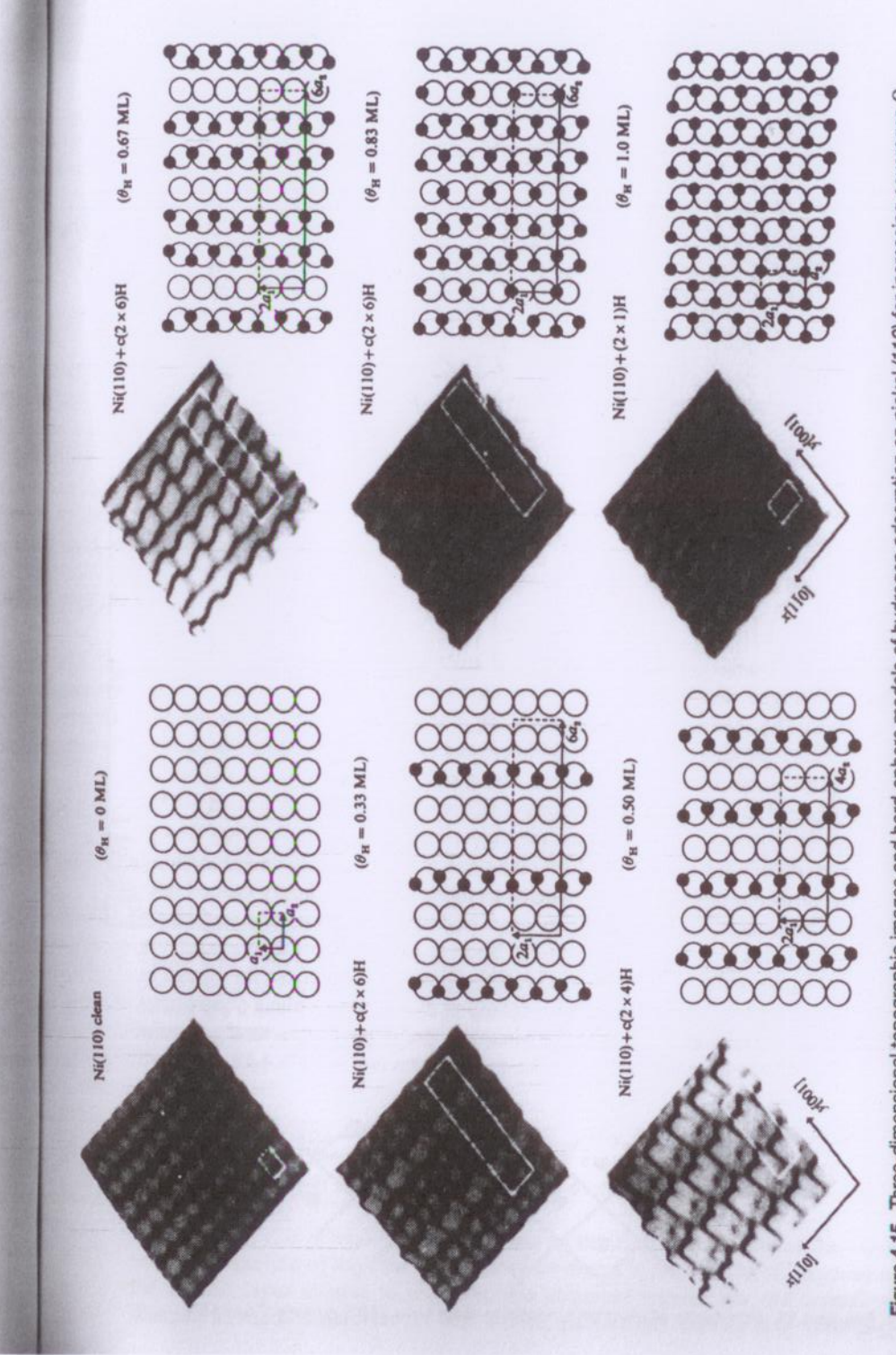
Figure 4.15 shows best-fit corrugation surfaces and hard-sphere models for atomic hydrogen adsorption on nickel (110) at different coverages as determined by helium atom scattering from the sample surface. The three-dimensional topographic images clearly indicate the surface layer symmetry and corrugation when compared to the clean nickel (110) surface. The hard-sphere models depict proposed surface structures that are consistent with the topographs and other experimental data. Unit cells for five different surface structures are shown on the hard-sphere models. Note the zig-zag pattern of hydrogen atoms and their highly anisotropic interactions on the nickel (110) surface.

Figure 4.16 depicts both commensurate and incommensurate ordered surface layers of krypton adsorbed on (0001) graphite. In the commensurate structure, the krypton adatoms occupy one of the three equivalent sites (labelled A, B and C) on graphite to form a  $\sqrt{3} \times \sqrt{3} - 30^\circ$  structure. As the surface coverage increases, the krypton atoms pack together to form a surface layer in which the atoms do not exhibit a unique binding site with respect to the underlying solid substrate. This type of surface layer is called incommensurate. This situation can occur for gas coverages near unity if the interadsorbate potential energy interactions that determine the lattice constant of the surface dominate over the adsorbate-substrate potential energy interactions.

Given the interaction between substrate and adsorbate atoms, the tendency for many substrates to reconstruct (as discussed in the next section) and the variation of the thermodynamic quantities with temperature, it is possible to imagine that there is a rich variety of phase transitions that can occur at surfaces. These are discussed in Section 4.5.

#### 4.4. SURFACE RELAXATION AND RECONSTRUCTION

In Section 4.2, we saw that the surface structure can vary from the ideal TLK model because thermodynamically stable defects are present and surfaces can roughen if they acquire sufficient thermal energy. In this section, we examine two additional ways in which actual surfaces may differ from the ideal hard-sphere model presented earlier. These two ways are by surface relaxation and surface reconstruction, both of which decrease the energy of an actual crystal surface compared to that of the simple hard-sphere broken-bond configuration. We also look at surface relaxations and reconstructions on f.c.c. metals, building on our previous treatments. In addition, we examine these phenomena on silicon surfaces to illustrate some of the differences that occur when crystals display highly directional bonding and because the surface structure of silicon is so important both scientifically and technologically. In relatively open structures such as ceramics and semiconductors, the energy changes associated with relaxation and reconstruction are usually much larger than those associated with roughening. This is less true for metal alloys, which are discussed first.



(110) for increasing coverages inted with the permission of Ca

Figure 4.16. (a) Commensurate and (b) incommensurate layers of krypton on graphite. The carbon atoms in graphite sit at the vertices of the hexagonal network and the large circles indicate the positions of adsorbed krypton atoms. The commensurate structure in (a) is a  $\sqrt{3} \times \sqrt{3} - 30^{\circ}$  structure where the adatoms occupy one of the three equivalent sublattices. From [10,45] reprinted with the permission of Cambridge University Press.

One way to envision relaxation at a metal surface is as follows. In metals, the positively charged ion cores are screened by symmetrical Wigner-Seitz charge clouds formed by the highly mobile conduction electrons [46]. This is illustrated in Figure 4.17 for the case of an f.c.c. crystal viewed along a <100> direction below. When a {100} surface is created, the electron distribution can be imagined to initially separate along the boundaries of the Wigner-Seitz cells as indicated by the solid lines in Figure 4.17. Once separated, the electrons at the surface are free to change their distribution in space to lower their energy, which results in a smoothing out of the surface electronic charge density, as indicated by the heavy dashed line. This smoothing out of the charge density gives rise to the formation of a surface dipole layer, as indicated by the + and – signs. Because of the surface dipole layer, the positive ion cores in the topmost atomic layer feel a net repulsion from the charge in their Wigner-Seitz cell and a contractive relaxation of the surface plane occurs until equilibrium is established. To first approximation, the in-plane structure generally retains the characteristics as the ideal close-packed structure. Figure 4.18 shows an

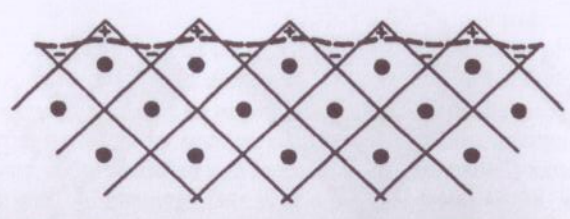


Figure 4.17. Schematic of electron smoothing at an f.c.c. (100) surface. From [47].

#### Cu(100) CHARGE DENSITY

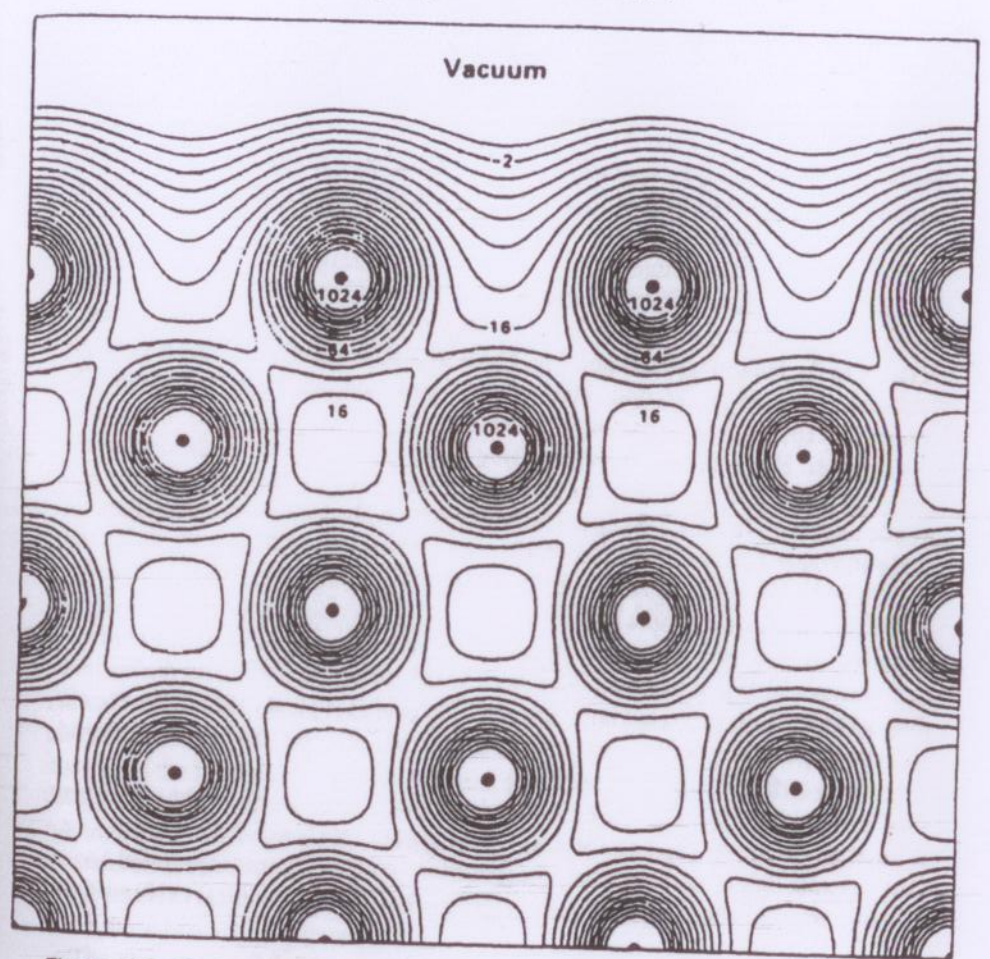


Figure 4.18. Conduction band charge density at a copper (100) surface, plotted on a (010) plane normal to the surface and passing through the centers of the atoms. Units of charge density are  $2.44 \times 10^{-3}$  electrons/bohr<sup>3</sup>. Charge densities on successive contours differ by a

actual charge density distribution at a copper {100} surface calculated using local-density functional theory [48]. Changes in the electronic structure are largely confined to the top layer of atoms and smoothing of the charge density at the surface is readily apparent.

In metals, it is often found that there is an oscillatory relaxation of the surface where contraction of the first layer of surface atoms is followed by an expansion of the second layer relative to the bulk; this sequence repeats into the crystal with damped strength. This behavior also can be qualitatively explained by referring to

Figure 4.17. When the atoms in the first surface layer find themselves in a medium with a lower average electron density than their bulk counterparts and contract inward, this contraction brings additional charge density into the neighborhood of the second layer of atoms. These atoms now find themselves on the high-density side of average. To lower the average electron density around them, the second layer exerts a force that pushes away the third layer of atoms (i.e., the second layer of atoms expands relative to the bulk spacing). The third layer then finds itself on the lower density side of average. This process continues and a damped oscillatory relaxation proceeds into the bulk.

Table 4.2 shows experimentally determined surface relaxations for the top three atomic layers in four different unreconstructed f.c.c.  $(1 \times 1)$  metal surfaces. The symbols  $\Delta z_{ij}$  indicate the change in the interlayer spacing  $\Delta z$  between layers i and j relative to the bulk interplanar spacing. These data show that the top layers generally display a small contraction relative to the bulk and, also, that the atomically rougher  $\{110\}$  surface shows larger relaxations than do the smoother  $\{100\}$  and  $\{111\}$  faces. Evidence for slight expansion in the second layer and the oscillatory behavior mentioned above is seen for most of the  $\{110\}$  surfaces. The values and trends shown in Table 4.2 compare favorably with embedded atom calculations of these and other f.c.c. metal surfaces [50].

A number of metal surfaces reconstruct in order to lower their surface energy rather than undergo a simple relaxation process as described above. Figure 4.19 illustrates two common types of reconstruction using a simple cubic lattice with lattice constant  $\alpha$ . When reconstruction occurs, the surface unit cell has dimensions that differ from the projected bulk unit cell. The gold (110) and (100) surfaces both reconstruct, and we examine the gold (110) surface in some detail to understand why metal surfaces might reconstruct.

Clean (110) surfaces of the f.c.c. metals iridium, platinum, and gold are known to reconstruct to a  $(1 \times 2)$  surface, whereas the clean surfaces of most other f.c.c. (110) metals do not undergo this reconstruction [49,50]. The reconstruction has a missing row geometry, where alternate close-packed rows of the ideal (110) surface

Table 4.2. Surface relaxations for several low-index surfaces of unreconstructed copper, nickel, gold and palladium\*

Surface	Relaxation	Cu	Ni	Au	Pd
(100)	$\Delta z_{12}$	-0.0020	-0.0156	0.0000	0.0050
	$\Delta z_{23}$	0.0031	0.0000	0.0000	0.0000
	$\Delta z_{34}$	0.0027	0.0000	0.0000	0.0000
(110)	$\Delta z_{12}$	-0.0108	-0.0050	-0.0125	-0.0080
	$\Delta z_{23}$	0.0029	0.0000	0.0070	0.0010
	$\Delta z_{34}$	0.0000	0.0000	-0.0025	0.0000
(111)	$\Delta z_{12}$	-0.0014	0.0000	0.0072	0.0000
	$\Delta z_{23}$	0.0000	0.0000	0.0000	0.0000
	$\Delta z_{34}$	0.0000	0.0000	0.0000	0.0000

<sup>\*</sup>The distances are expressed in nanometers relative to the bulk interplanar spacing [49].

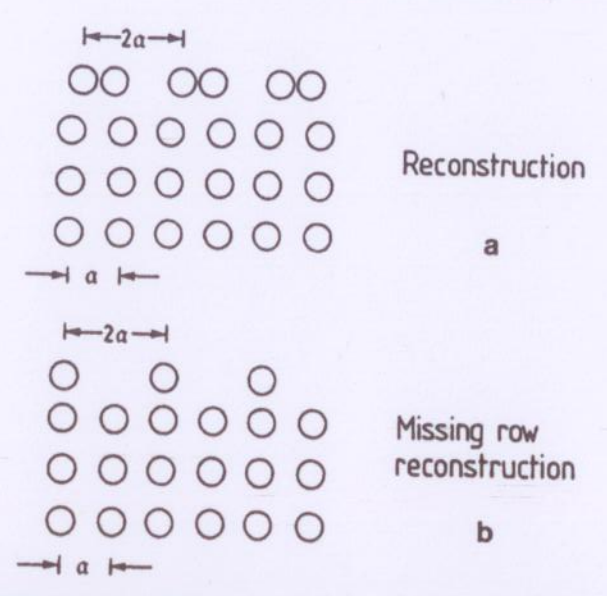


Figure 4.19. Schematic side view of the surface atoms of a simple cubic lattice with lattice parameter  $\alpha$ , where there is (a) reconstruction of the top atom layer into a surface net with a double periodicity  $2\alpha$ , and (b) a missing row reconstruction with missing atoms in the top plane. From [47] copyright Springer-Verlag.

are removed, thus forming narrow (111) facets. The reconstruction has been observed experimentally by several different techniques, with STM and HRTEM being two of the most direct. Figures 4.20 and 4.21 show STM and HRTEM images of the gold (110) ( $1 \times 2$ ) reconstructed surface, respectively. The crystallography of the surface is shown with the STM image in Figure 4.20 and a schematic of the reconstructed surface viewed along the [ $\bar{1}10$ ] direction is also shown for comparison. Three-atom (111) facets associated with the reconstructed surface are readily visible in the schematic in Figure 4.20.

The energetics of the missing row (1 x 2) reconstruction on (110) surfaces of nickel, palladium, platinum, copper, silver and gold were investigated using the embedded atom method [50]. In this study, the detailed geometry of the relaxed missing row structure and the relative energies of the relaxed missing row and unreconstructed surfaces were calculated and compared. Table 4.3 compares the surface energy difference between the reconstructed missing row surface and the unreconstructed (110) surfaces in their unrelaxed and fully relaxed geometries. The difference between the surface energies of the reconstructed and unreconstructed surfaces is only slightly changed by the relaxation in the atomic positions, indicating that the surface geometry is not determined by differences in the ability of the two surface geometries to lower their energy by relaxation. The surface energy difference between the reconstructed and unreconstructed surfaces is clearly largest for gold and palladium and is generally 20–50 mJ/m² less in the reconstructed geometry. Analysis of the detailed atomic positions associated with the (110) (1 × 2) re-

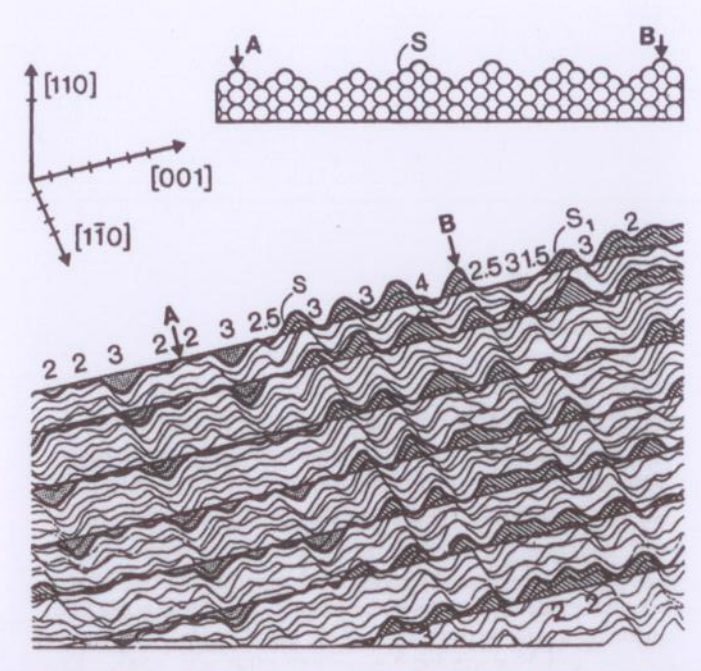


Figure 4.20. STM profile of a gold (110) (1  $\times$  2) reconstructed surface. The divisions on the crystal axes represent 0.5 nm. The straight lines help visualize the terraced structure with monolayer steps and the numbers on the top scan give distances between maxima and minima in units of the bulk lattice spacing. The inset shows the proposed structural model for the corrugation between A and B. From [10] reprinted with the permission of Cambridge University Press and [51] reprinted with kind permission from Elsevier Science-NL, Amsterdam, The Netherlands.

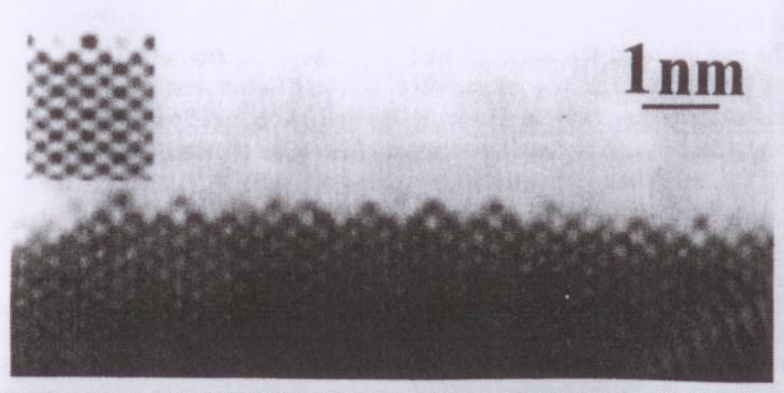


Figure 4.21. Experimental HRTEM image along a <110> direction showing the  $(1 \times 2)$  reconstructed surface on gold (110). A simulated image of the surface is shown in the inset. From [52].

Table 4.3. Surface energy difference  $\Delta \gamma^{\rm SV} = \gamma^{\rm SV}_{\{1\times 2\}} - \gamma^{\rm SV}_{\{1\times 1\}}$  between the reconstructed missing row surface and unrelaxed and relaxed unreconstructed (110) surfaces of various f.c.c. metals\*

Metal	$\Delta \gamma^{SV}$ (unrelaxed)	Δγ <sup>SV</sup> (relaxed	
Cu	19.2	17.6	
Ag	-8.0	-6.4	
Au	-36.8	-28.8	
Ni	22.4	20.8	
Pd	-9.6	-6.4	
Pt	-46.4	-33.6	

<sup>\*</sup>The energies are in units of mJ/m2 (from [50]).

construction showed that the preferred  $(1 \times 2)$  structure results from a competition between attractive pair interactions at second-nearest-neighbor atomic distances and repulsive three-body interactions at nearest-neighbor distances. The results also showed that the energy of the reconstructed surface decreases relative to the unreconstructed surface as one goes down the columns in the periodic table, consistent with the observation that only elements at the bottom of the periodic table such as gold and platinum reconstruct.

Qualitatively, one might argue that the  $(1 \times 2)$  reconstruction occurs as a trade-off between the formation of a unit area of  $\{110\}$  surface with a surface energy  $\gamma^{\text{SV}}_{\{110\}}$  and the same projected surface area composed of microfacets of  $\{111\}$  surface with surface energy  $\gamma^{\text{SV}}_{\{111\}}$ . For example, the atomic model at the top of Figure 4.20 displays  $\{111\}$  facets approximately three atoms wide. As mentioned in Section 3.5.2, a high-index surface may be unstable with respect to faceting; Figure 4.20 is an atomic illustration of such a situation. Problem 4.10 compares the energy of the unreconstructed  $\{110\}$  surface with that of the reconstructed surface with  $\{111\}$  microfacets using a nearest-neighbor bond model. The answer to this problem shows that the two surfaces have the same surface energy in the nearest-neighbor model, and, hence, it cannot be used to determine the most stable structure. The longer-range interactions included in the EAM are able to reveal these small energy differences, as discussed above.

The situation for reconstruction of silicon surfaces (and other directionally bonded crystals) is somewhat different than that for metals. This difference deserves further discussion because it is quite important in understanding the nature of surface reconstruction. When the strong, directional bonds of silicon are broken at a surface the atoms are in a very unstable state. In response, they undergo high elastic distortion and rearrange to form a new structure with fewer dangling bonds. This leads to a significant reduction in the surface energy as described further below.

Figures 4.22a and b show top and side views of the silicon (100) surface before and after reconstruction, respectively [53]. Because of the tetrahedral coordination in silicon, the surface atoms have two dangling bonds pointing out of the (100) surface. These bonds each contain an unpaired electron and are highly unstable. To satisfy partially these unpaired electrons, silicon dimer formation occurs, as illustrated

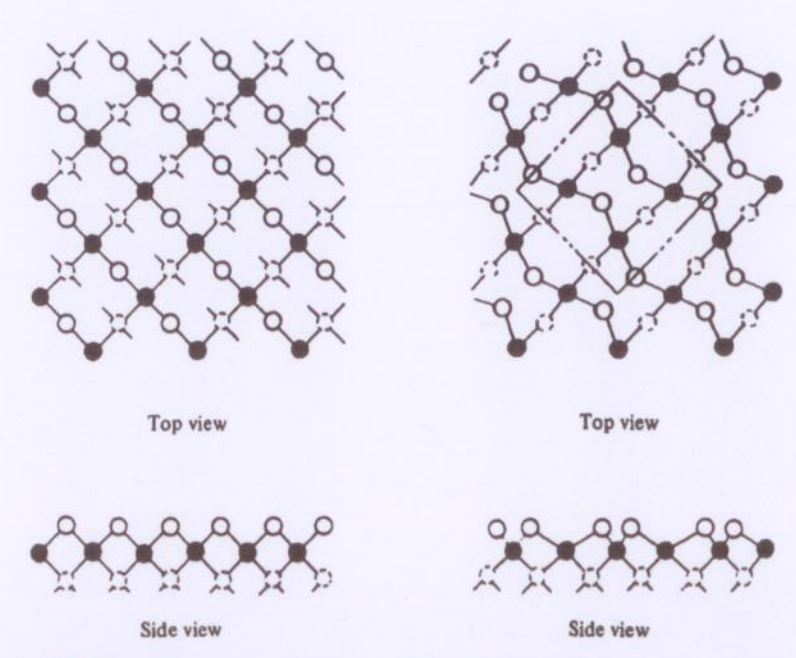


Figure 4.22. Top and side views of a silicon (100) surface (a) before and (b) after dimer formation and reconstruction to a  $(2 \times 2)$  lattice. From [53] reprinted with the permission of Cambridge University Press.

in Figure 4.22b. Dimer formation also occurs on the other low-index silicon surfaces such as {111} and {110}, and this greatly reduces the surface energy [47].

Table 4.4 compares many-body calculations of the surface energies of unreconstructed and reconstructed silicon surfaces in both unrelaxed and fully relaxed configurations  $\gamma_{\text{many-body}}^{\text{SV}}$  with the surface energies based on the nearest neighbor broken-bond model  $\gamma_{\text{nn}}^{\text{SV}}$ . The number of broken bonds per atom  $n_b$  on each surface and the bond energy per atom pair  $-\epsilon_b$  are also shown. Note that reconstruction of the silicon  $\{100\}$  surface to either the  $(1 \times 2)$  or  $(2 \times 2)$  configuration reduces the surface energy by almost a factor of two compared to the nearest-neighbor calculation.

Table 4.4. Calculated surface energies (in mJ/m²) for silicon

Source: From [53].

	$n_{b}$	−e <sub>b</sub> (eV)	$\gamma_{nn}^{SV}$	γ SV many-body	
Plane				Unrelaxed	Relaxed
{111} unrecon.	0.5	0.58	1465	1225	1019
{110} unrecon.	1.0	1.17	1794	1601	1468
{100} unrecon.	2.0	2.34	2537	2310	2220
$\{100\} - (2 \times 1)$					1434
$\{100\} - (2 \times 2)$					1243

Even in the fully relaxed many-body calculation, the surface energy of the  $(2 \times 2)$  reconstructed surface is less than that of the unreconstructed relaxed surface by approximately  $1000 \text{ mJ/m}^2$ . This is a much greater reduction than the approximately  $40 \text{ mJ/m}^2$  reduction observed for reconstruction of the gold (110)  $(1 \times 2)$  surface, for example, emphasizing the large reduction in energy that can be gained by reconstruction of semiconductor surfaces with directional bonds as compared to metal surfaces. Similar reconstructions occur with dangling bonds at the edges of ledges on silicon surfaces and these also lead to major reductions in the excess energy of the ledges.

Figure 4.9 showed an STM image of monatomic ledges on a silicon  $\{100\}$  surface that had reconstructed to a  $(1 \times 2)$  configuration. When a monatomic step occurs on a silicon  $\{100\}$  surface, its height is equal to one quarter of the bulk lattice constant from the tetrahedral bonding in the diamond cubic (d.c.) structure. Thus, the 90° rotation of the  $(1 \times 2)$  rows that occurs on alternate terraces as in Figure 4.9 is a direct consequence of the symmetry of the d.c. structure; that is, it can be thought of as two interpenetrating f.c.c. lattices rotated 90° relative to one another each quarter of the lattice spacing along the <100> direction. As mentioned earlier with regard to Figure 4.9, the energy of the ledges that run parallel to the dimer rows is approximately one-third of those that run perpendicular to the dimer rows.

Another well-known reconstruction on silicon is the (7 × 7) reconstruction that occurs on the (111) surface. This very complex surface reconstruction solves the problem of high-energy dangling bonds by eliminating many of them entirely. Figure 4.23 shows a transmission electron diffraction pattern obtained from the silicon (111) (7 × 7) surface. Such data and electron microscope images led Takayanagi et al. [54] to propose a complicated reconstruction for this surface, which has since been verified by other techniques including surface X-ray scattering, photoemission spectroscopy and STM [55]. The key structural features of this surface model, which is shown in projection normal to the surface in Figure 4.24, are the following:

- 1. Twelve top layer adatoms
- 2. A stacking fault in one of the two triangular subunits of the second layer
- 3. Nine dimers that border the triangular subunits in the third layer
- 4. A deep vacancy at each apex of the unit cell.

On a normally terminated silicon (111)  $(7 \times 7)$  surface, there is one dangling bond on each of the 49 top-layer atoms. The purpose of the stacking fault in one triangular subunit of the second layer of atoms in the unit cell is to eliminate seven atoms along the row where the faulted subunit is matched to the unfaulted subunit. Hence, there are only 42 atoms (and dangling bonds) in what is now the second layer of the reconstructed surface. One can then replace three dangling bonds by one, by allowing single silicon atoms (ejected from the original top layer or migrating from elsewhere) to adsorb and bond tetrahedrally to three second-layer atoms each. The 12 top-layer adatoms on the  $(7 \times 7)$  surface then reduces the number of dangling bonds to 18, or approximately one-third of the original number. A counterpart to this type

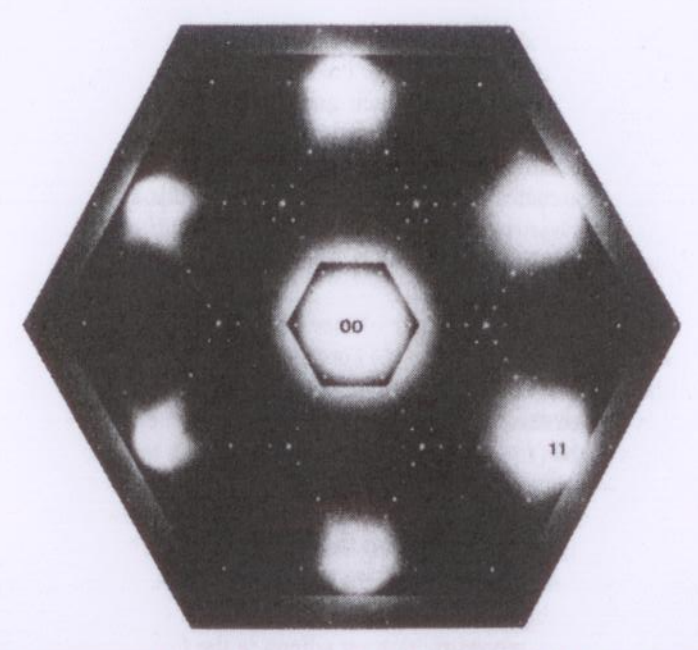


Figure 4.23. Transmission electron diffraction pattern for the silicon (111) ( $7 \times 7$ ) surface. The 00, 01 and 11 spots for silicon are labeled in the figure. From [10] reprinted with the permission of Cambridge University Press and [54] reprinted with kind permission from Elsevier Science-NL, Amsterdam, The Netherlands.

of very complicated surface reconstruction is not found on {111} metal surfaces because of the nondirectional nature of the metallic bond.

Striking STM images of the silicon (111) ( $7 \times 7$ ) surface have been obtained and Figure 4.25 shows an example of these. The image in Figure 4.25a is a conventional topographic image that provides a view of the surface adatoms and the basic unit cell (outlined). The succeeding images in Figs. 4.25b through d display spatial variations in the tunneling current (brighter areas denote greater current flow) for different bias voltages. The image in Figure 4.25b was obtained for a surface state 0.35 eV below the Fermi level. This state is localized on the 12 adatoms but exhibits a distinct asymmetry between the faulted and unfaulted portions of the unit cell. The third image in Figure 4.25c shows a state 0.8 eV below the Fermi level that arises from the dangling bonds of the six second-layer atoms that are not directly bonded to adatoms. Note also the dangling bonds at the deep corner holes. The last image (Figure 4.25d) represents a deep state that probably corresponds to  $3p_x$  and  $3p_y$  orbitals of the adatoms bonded to  $3p_x$  orbitals of the atoms directly below them.

#### 4.5. PHASE TRANSFORMATIONS AND SURFACE MELTING

We discussed the concept of phase transformations in terms of a bulk system in Chapter 2. Here we examine the possibility of two-dimensional phase transforma-

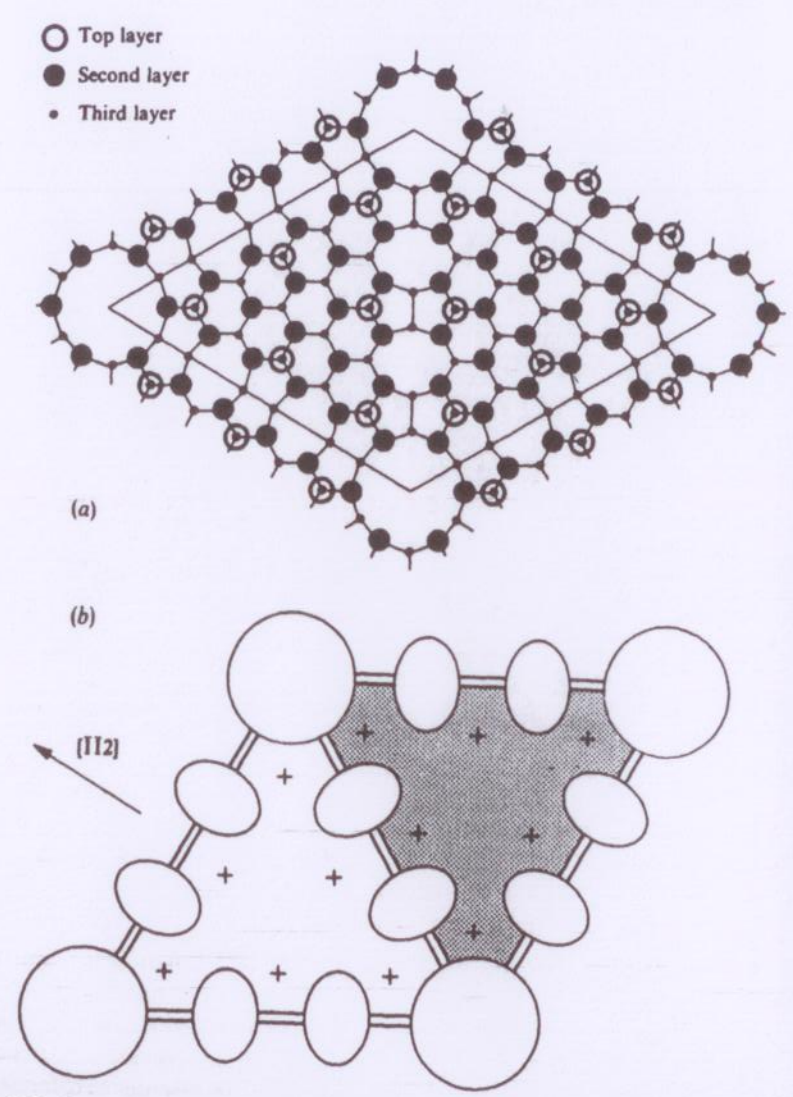


Figure 4.24. Surface structure of silicon (111) ( $7 \times 7$ ). (a) The first three layers of atoms, as seen from above, are labeled and the surface unit cell is outlined. (b) A schematic view that indicates the prominent depressions in the surface (round and oval holes), the dimers (double lines) and the stacking fault (shaded region). From [10] reprinted with the permission of Cambridge University Press and [56,57] reprinted with kind permission from Elsevier Science-NL, Amsterdam, The Netherlands.

tions at a surface. For a pure substance, these transformations include reconstruction and surface melting. When adsorption or segregation occurs to the surface, more complex reactions can occur. We begin our discussion with phase transformations and conclude with the concept of surface melting.

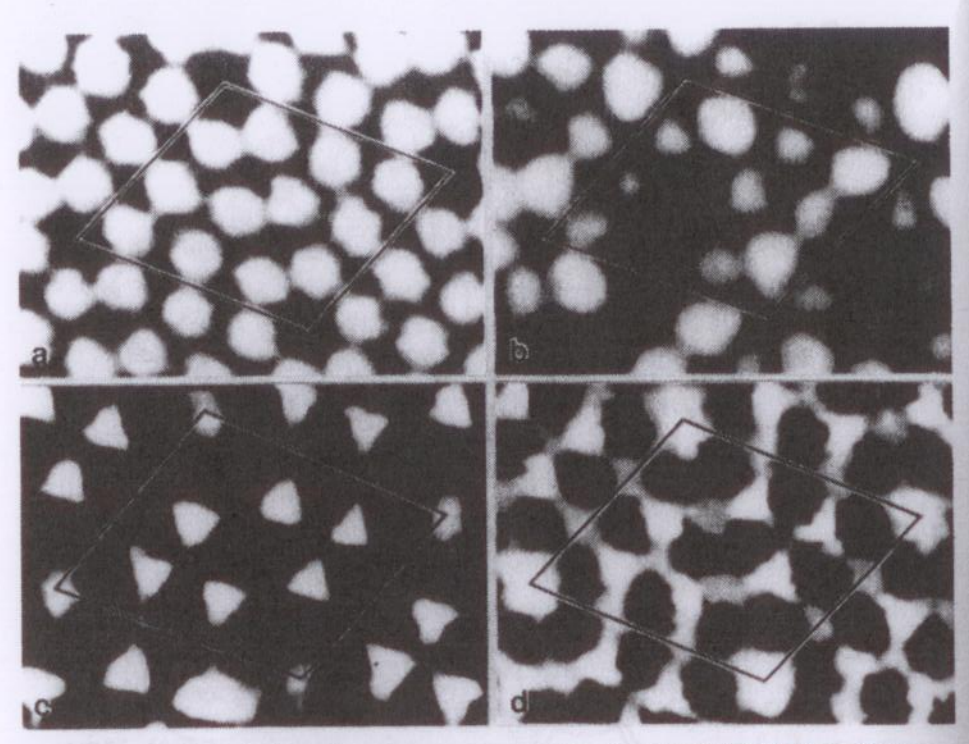


Figure 4.25. Scanning tunneling microscope images of the topography (a) and three electronic surface states (b)–(d) of a silicon (111) ( $7 \times 7$ ) surface. From [10,55] reprinted with the permission of Cambridge University Press.

#### 4.5.1. Surface Phase Transformations

It is often useful to characterize the competing phases in a transformation in terms of an order parameter. By convention, the order parameter usually has a nonzero value in one phase (usually the low-temperature low-symmetry state) and vanishes in the other (high-temperature high-symmetry) phase. We previously encountered the order parameter in Section 2.6. when discussing order-disorder transformations, for example. As illustrated in Figures 2.12 and 2.13, the order parameter usually displays two rather different types of behavior near the transformation temperature T<sub>c</sub>. A discontinuous change occurs in the order parameter for a first-order transformation. In a simple case, two independent free-energy curves cross one another as the temperature changes and the system abruptly changes from one distinct equilibrium phase to another. First-order phase transformations exhibit the familiar phenomena of phase coexistence and nucleation and growth. In contrast, in a continuous phase transformation, two competing phases become indistinguishable at To. In this case, the order parameter rises smoothly from zero as the temperature is lowered (Fig. 2.12). One typically finds that the order parameter in a continuous transformation varies as  $(T-T_c)^n$  for T very near  $T_c$ , where n is referred to as the critical exponent. As it turns out, the value of n only depends on a few physical properties such as the symmetry of the system, the dimensionality of the order parameter (i.e., scalar versus vector) and the dimensionality of space. This suggests that rather interesting things may happen at a surface where the dimensionality is two rather than three.

It is found that solid surfaces undergo a variety of reconstructive phase transformations as a function of temperature. Thus, we would like to display a structural phase diagram for surfaces as we would do for the analogous bulk problem. Unfortunately, it is often difficult to establish the true surface structure, and additionally, many surface phases are actually metastable, which complicates determination of the equilibrium structural phase diagram. In spite of these problems, a number of surface phase transformations have been examined in detail, and we will look at several, starting with a continuous transformation in the familiar f.c.c. metal gold, continuing with a first-order phase transformation in silicon, and then closing by looking briefly at some phase transformations than can occur for an asorbed surface layer on a substrate, returning to the example of krypton on graphite in Figure 4.16.

The  $(2 \times 1) \rightarrow (1 \times 1)$  reconstructive phase transformation that occurs for a gold (110) surface provides an excellent example of a continuous surface transformation. Experiments show that the high-temperature  $(1 \times 1)$  structure reversibly transforms to the missing row  $(2 \times 1)$  structure depicted in Figures 4.20 and 4.21 at approximately 377°C. Based only on the symmetry of the (110) surface, it is possible to predict that the temperature dependence of the order parameter near  $T_c$  should exhibit a value of the critical exponent n = 1/8 in accordance with the exact result of Onsager [58]. As shown by the experimental data in Figure 4.26, obtained by monitoring the intensity of superlattice reflections unique to the  $(2 \times 1)$  phase by low-en-

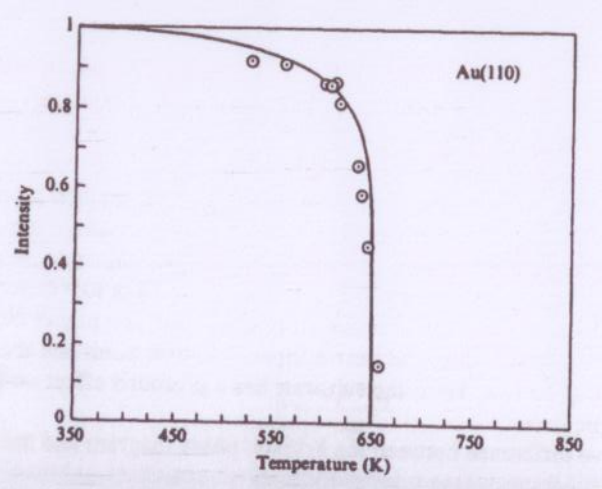


Figure 4.26. Temperature dependence of the order parameter for the  $(2 \times 1) \rightarrow (1 \times 1)$  transformation on gold (110). The intensity of the  $(2 \times 1)$  LEED spots (circles) are compared with Onsager's exact solution of the two-dimensional Ising model (solid curve). From [10,59] reprinted with the permission of Cambridge University Press.

ergy electron diffraction (LEED), the order parameter goes continuously to zero with an experimental value of  $n = 0.13 \pm 0.02$ , very close to Onsager's solution. The EAM combined with Monte Carlo calculations has been used to examine the detailed structure of the gold (110) surface near  $T_c$  [60]. The picture that emerges is that below the critical temperature, the rows are generally long and coordinated, with some defects present, whereas above the critical temperature, some short-range order persists in the form of short chains of atoms along the  $<1\overline{10}>$  direction with little coordination among the rows.

The silicon  $(1 \times 1) \rightarrow (7 \times 7)$  reconstruction is an example of a surface phase transformation that exhibits the characteristics of a first-order phase transformation and cannot proceed by a continuous transformation according to symmetry considerations [10]. Figure 4.27 shows a series of reflection electron microsope (REM) images that clearly demonstrate that the reaction is first-order [61]. The images show the nucleation and growth of regions of  $(7 \times 7)$  reconstruction as the sample is cooled below the transformation temperature. The complete transformation occurs over a range of 20° to 30°C below  $T_c$ . This sluggish behavior is not uncommon for first-order phase transformations where strain plays an important role in the transformation [62].

Before discussing surface melting, we examine the possibility of phase transformations involving adsorbed atoms onto a surface, a situation that was introduced but not fully explored in Section 4.3. This discussion introduces the concept of epitaxy, or lattice matching between a substrate and an overlayer. In particular, we compare the argon-graphite, krypton-graphite and xenon-graphite systems shown in Figure 4.28. It is important to note from the onset, that the bulk phase diagrams for argon, krypton, and xenon are essentially identical and all three elements are f.c.c. in the solid state. The variation that occurs among the phase diagrams in Figure 4.28 is thus due to the interaction of the adsorbates with the substrate and each other. The interaction involves weak attraction from the dispersion forces and hard core repulsion, similar to Figure 1.1. Of the three phase diagrams, only xenon exhibits a typical bulklike topology with regions of two-phase coexistence of gas (G) + liquid (L), gas + solid (S), and liquid + solid, in addition to a well-defined triple point and critical point. The solid, however, is crystallographically incommensurate with the substrate, as illustrated previously in Figure 4.16b. A similar incommensurate solid (IS) is found for argon although its phase diagram lacks a region of solid-liquid coexistence (or it is very small). Only krypton exhibits a legitimate commensurate solid (CS) phase with a  $\sqrt{3} \times \sqrt{3} - 30^{\circ}$  unit cell at low density (Figure 4.16a), but a transition to an incommensurate phase occurs at a higher coverage. In addition, krypton does not appear to have a triple or critical point and the CS melts directly to a fluid (F) phase. Thus, the substrate has a profound effect on the behavior of these simple gases.

The qualitative difference between the krypton phase diagram and the other two inert gas phase diagrams arises principally from an adsorbate–substrate size mismatch effect. To see this, we can calculate the fractional difference between the inplane graphite lattice constant and the bulk solid phase lattice constants of argon, krypton, and xenon. This quantity is commonly called the misfit  $\delta$  and is given as

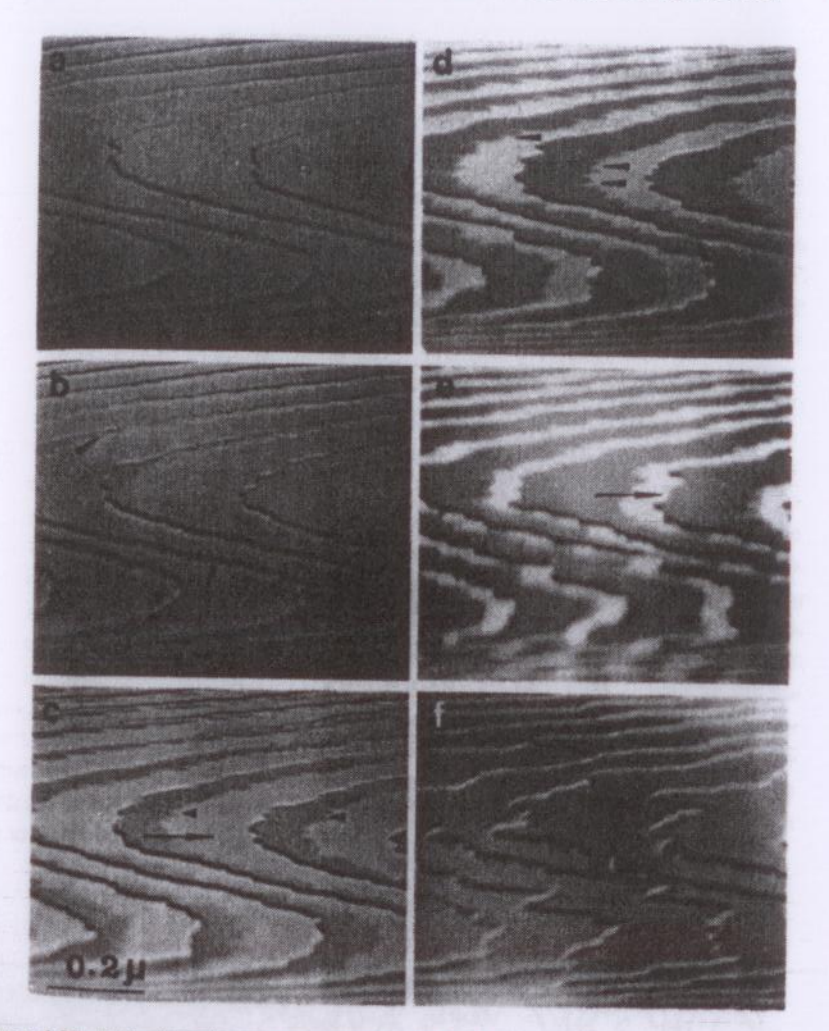


Figure 4.27. Reflection electron micrographs of the  $(1 \times 1) \to (7 \times 7)$  transformation upon cooling of a stepped silicon (111) surface. (a) Initial (1×1) structure and (b)–(e) regions of (7×7) structure (dark) nucleate at the top of monatomic steps and expand across the terraces. The full arrows in (c) and (e) indicate the direction of growth and (f) shows the completed  $(7 \times 7)$  structure. Reprinted from [61] with kind permission from Elsevier Science-NL, Amsterdam, The Netherlands.

$$\delta = \frac{\alpha_{\rm f} - \alpha_{\rm s}}{\alpha_{\rm s}}.\tag{4.21}$$

where  $\alpha_r$  is the lattice constant of the film or surface layer, and  $\alpha_s$  is the lattice constant of the substrate. The values for argon, krypton, and xenon expressed in percent misfit ( $\delta \times 100$ ) are -8%, -5% and +8%, respectively. Therefore, the slightly undersized krypton atoms are able to form a commensurate surface layer by occupying

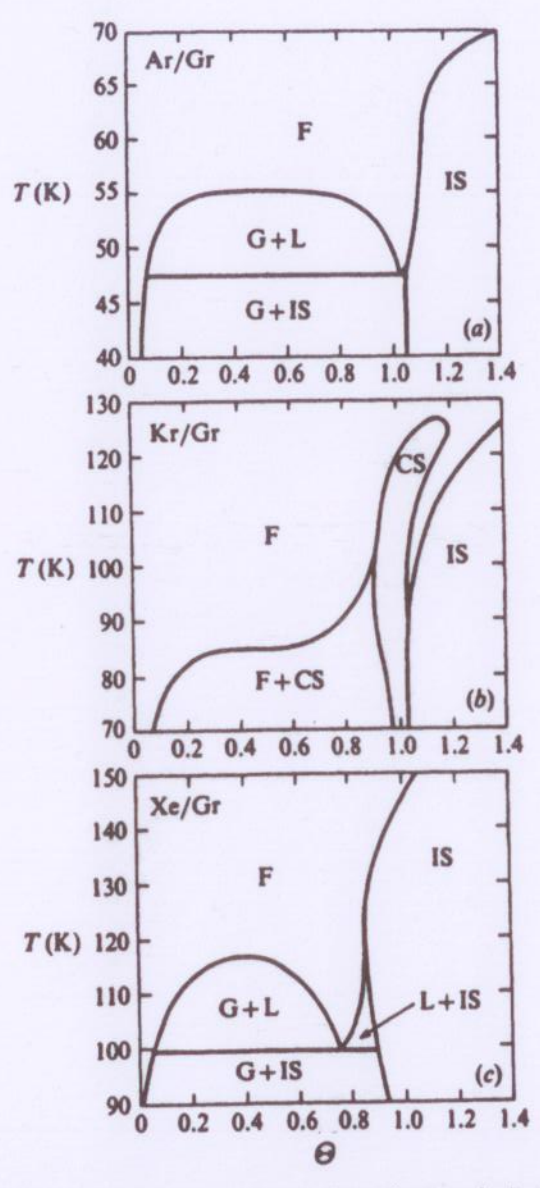


Figure 4.28. Equilibrium temperature—coverage phase diagrams for inert gases on graphite:
(a) Ar, (b) Kr and (c) Xe. The symbols are explained in the text. From [10] reprinted with the permission of Cambridge University Press.

the hexagonal sites on the regular graphite lattice over a wide range of coverage (Figure 4.28b). These sites are within -5% of the minima of the krypton-krypton interaction potential. This condition is less well satisfied for the more undersized argon and oversized xenon atoms, and they reduce their energy by ignoring the favorable adsorption sites on the graphite substrate and adopting their own (natural) lat-

tice constant. This feature has been confirmed by X-ray diffraction [10] and implies that the surface layer ignores the substrate and essentially floats on top of the graphite as though it were truly two-dimensional.

Another interesting aspect of the krypton-graphite phase diagram is the possiblity of having a commensurate-incommensurate phase transformation with increasing adsorbate coverage. In the vicinity of the C-I phase transformation, the krypton surface layer can be viewed as a collection of commensurate regions separated by localized regions of high atomic density called domain walls or solitons. (This is analogous to the concept of dislocations in crystalline interfaces discussed in Part IV.) A schematic illustrating domain walls between three commensurate regions occupying A, B and C positions on the graphite substrate is shown in Figure 4.29. Molecular dynamics simulations of the krypton-graphite structure at a density just slightly in excess of the C-I phase boundary ( $\Theta = 1.028$ ) are shown in Figure 4.30. The white regions in Figure 4.30 correspond to areas where the krypton atoms are associated with a particular graphite sublattice. The dark regions are the domain walls, where krypton atoms effectively straddle maxima in the graphite potentials, as illustrated in Figure 4.29. At the low temperature shown in Figure 4.30a, the commensurate domains are hexagonally-shaped. In contrast, at the higher temperature in Figure 4.30b, the domain walls are frayed and wander significantly as though a fluid phase were creeping in between the CS and IS phases. As the temperature continues to increase, the C-I transition proceeds in a gradual continuous manner with the width of the domain walls increasing and the separation between the domain walls decreasing. Eventually, the entire layer disorders and becomes incommensurate. This behavior is plotted in Figure 4.31. The transformation is continuous with a critical exponent of approximately a third. Note the similarity of this behavior to that of ledge roughening in Figure 4.10 and Eq. (4.15).

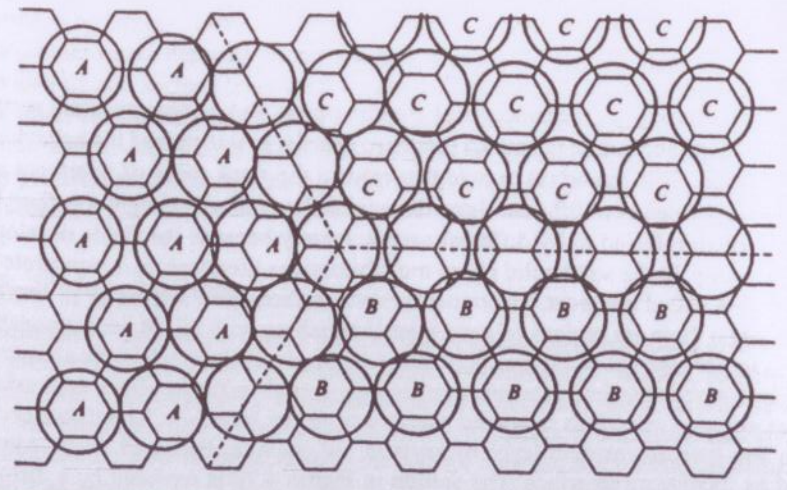
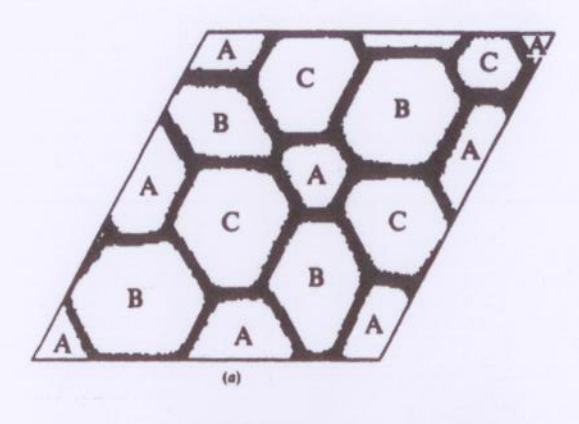
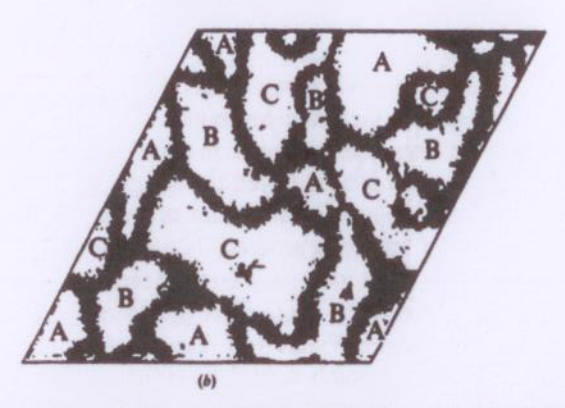


Figure 4.29. Schematic of a wall intersection where three commensurate domains of krypton on graphite meet. From [10,45] reprinted with the permission of Cambridge University Press.





**Figure 4.30.** Illustrations of the crystallographic structure of two-dimensional krypton on graphite obtained by molecular dynamics simulations of about one monolayer coverage. The depicted rhombus is 62 nm on each side and the temperature is (a) 17 K and (b) 95 K. From [10.63] reprinted with the permission of Cambridge University Press.

We have introduced the concepts of commensurate and incommensurate surface layers, solitons and lattice mismatch (epitaxy) in order to understand the behavior of surface layers. It is important to note that exactly the same types of interfaces and defects exist when two different three-dimensional solids are brought together, but they are often referred to by different names, mainly because the fields developed independently. In the solid-solid phase transformations literature, commensurate interfaces are called coherent, incommensurate interfaces are referred to as semicoherent when there are regions of good atomic matching with misfit accommodating defects in between (as in Figures 4.29 and 4.30), or incoherent when the atomic interactions across the interface are significantly less than those within each of the phases and any mismatch is spread evenly across the interface. The interface between the incommensurate layer of krypton on graphite discussed above can be called an incoherent interface. The soliton in Figure 4.29 is replaced by a dislocation in three dimensions. It is also worth emphasizing that whether the interface

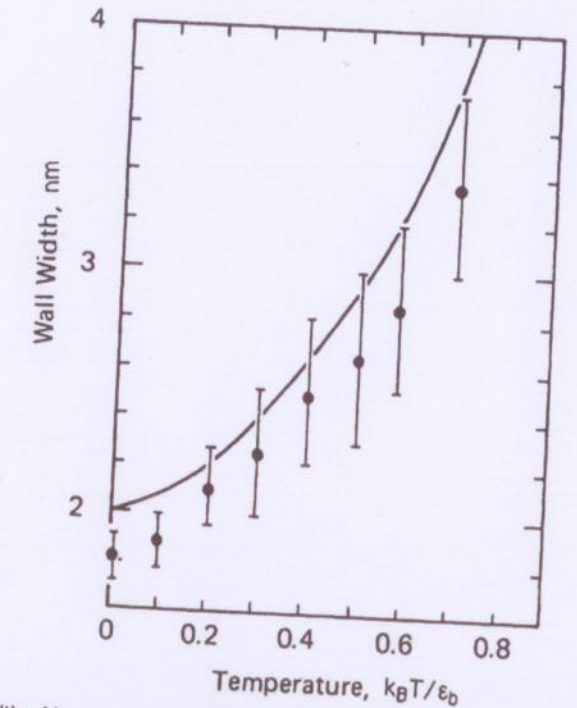


Figure 4.31. Width of incommensurated domain walls as a function of temperature for krypton on graphite, normalized by  $k_{\rm B}/\epsilon_{\rm b}$ , where  $\epsilon_{\rm b}$  is the bond energy of the krypton atoms. The dots with error bars are the data taken from snapshots of the molecular dynamics simulations and the solid line is a result from a theoretical calculation. Reprinted from [63] with kind permission from Elsevier Science-NL, Amsterdam, The Netherlands.

chooses to be largely commensurate with regions separated by solitons or completely incommensurate depends on the magnitude of the interaction potentials between the substrate and surface layer versus those within the layer itself. This concept applies when considering whether an interface between three-dimensional metal and ceramic solids will choose to be semicoherent or incoherent, for example. Thus, many parallels exist between the surfaces we are considering here and other types of interfaces.

### 4.5.2. Surface Melting

At sufficiently high temperatures, reconstructive phase transformations give way to a different class of equilibrium surface phase transformations, namely, roughening and melting. The roughening transformation was discussed previously in Section 4.2. This transformation is characterized by a temperature at which the free energy of a monatomic step vanishes. In this section we consider the melting transformation of a surface.

Melting is a familiar first-order phase transformation. At the bulk melting point

 $T_{\rm m}$ , discontinuities occur in the thermodynamic variables as the symmetry abruptly changes from that of a crystalline space group to the rotationally invariant state of a liquid. A simple estimate of  $T_{\rm m}$  comes from the Lindemann criterion [64,65], which states that the crystal melts when the atomic mean square displacement due to thermal vibrations  $< u^2 >$  is a significant fraction ( $\sim 15\%$ ) of the lattice constant. As demonstrated in Problem 4.12, in the Debye model,

$$\langle u^2 \rangle = 3 \hbar^2 T_{\rm m} / m k_{\rm B} T_{\theta}^2$$
 (4.22a)

and thus

$$T_{\rm m} \cong ({\rm constant}) \, m T_{\theta}^2,$$
 (4.22b)

where m is the atomic mass,  $\hbar = h/2\pi$ , and h is Planck's constant,  $k_{\rm B}$  is Boltzmann's constant, and  $T_{\rm \theta}$  is the Debye temperature. Equation 4.22b shows that the melting temperature increases proportional to the atomic mass and Debye temperature. We can rationalize this behavior in terms of a simple bonding model by noting that it takes more thermal energy to move heavier atoms that are strongly bonded. Note that this is the same relationship expressed in Figure 3.6 between the Debye temperature and surface energy, which again relates back to the strength of the interatomic bonds.

Diffraction experiments can measure the mean square atomic displacement directly because thermal vibrations attenuate the diffracted intensities by the so-called Debye—Waller factor. Therefore, comparison of X-ray and LEED data for the same specimen reveals the relative amplitude of thermal vibrations at the surface as compared to the bulk. Typically, experiments of this type show that the thermal excursion of surface atoms perpendicular to the surface is 50% to 100% greater than a bulk atom at the same temperature. The lower value follows intuitively if we imagine that a surface atom only experiences half of the restoring force of a bulk atom.

Simple application of the Lindemann criterion suggests that surface atoms should disorder (melt) at a significantly lower temperature than the bulk melting temperature. Further, if a disordered layer forms at the surface, then this layer should exert a perpendicular restoring force on the second layer that is intermediate between that of an ordered surface layer and the vacuum. Thus, the second layer should melt at a slightly higher temperature than the surface but still lower than the bulk. A similar argument applies to succeeding layers inward so that the melt front propagates into the crystal with increasing temperature as each layer melts when its Lindemann criterion is met, until the entire process is complete at  $T_{\rm m}$ .

Confirmation of this idea is shown in the molecular dynamics simulations for a silicon (100) ( $1 \times 1$ ) surface using an interaction potential appropriate to silicon in Figure 4.32 [10]. At moderate temperatures in Figure 4.32a, all the atoms in planes parallel to a free (100) surface exhibit small harmonic displacements around their equilibrium positions. At an elevated temperature still below the bulk melting point in Figure 4.32b, one clearly sees a disordered surface layer. It is interesting to note that this layer is not completely disordered and that the underlying ordered layers in-

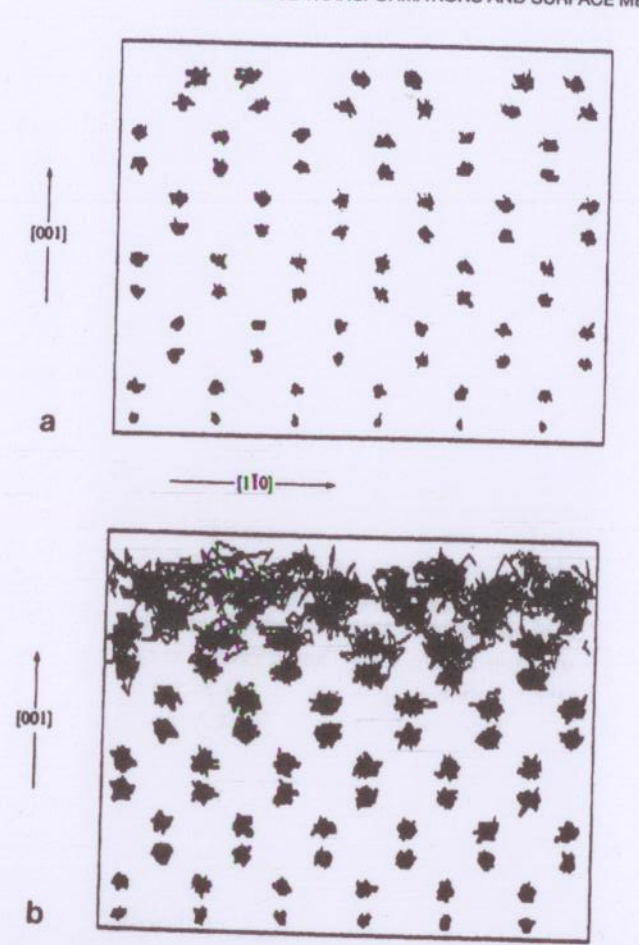


Figure 4.32. Particle trajectories from a molecular dynamics simulation of silicon (100) viewed along a <110> direction at (a) 1003 K and (b) 1683 K. (It is important to note that the bulk meltitis temperature exactly.) From [10].

duce some residual short-range order into the melted region. The melt front was observed to move into the crystal as the temperature was raised as suggested above.

Similar molecular dynamics calculations performed using a Lennard–Jones potential have shown the same behavior [66]. In addition, these studies also explored the orientational dependence of surface melting and found that the resistance to surface melting decreased in the order {111}, {100} to {110}, just as we might expect from our simple nearest-neighbor broken-bond model, where the {111} surface has the fewest broken bonds and is the most stable, while the {110} surface has the most broken bonds and is the least stable. The surface layers were also observed to contain a density deficit that was maximum at the surface and decreased with distance into the surface, again just as we would expect from the results discussed in

Section 4.2.2. Thus, there is now strong theoretical and experimental evidence to suggest that surface melting readily occurs on many solid surfaces. The mechanisms by which melting occurs in bulk solids are less clear.

#### 4.6. PARTICLE SIZE, SURFACE STRESS AND STABILITY

When a phase is small, the surface energy can have a significant effect on certain thermodynamic properties of the phase. For example, the pressure inside a tiny liquid drop or crystal is higher than in the surrounding vapor, increasing the vapor pressure of the drop or crystal. Similarly, bumps or depressions on a surface have a different internal pressure and vapor pressure than a flat surface. In this section, we look at the effects of particle size and interface curvature on the properties of surfaces. These concepts apply to solid, liquid and vapor phases. For simplicity, we begin our discussion by considering a liquid drop in equilibrium with its vapor and then extend the discussion to include crystalline particles.

If we take the case of a spherical liquid drop, we can consider the surface energy as a surface pressure that is exerted tangentially along the surface and then consider the role of the external and internal pressures which act normal to the surface on its properties, as illustrated in Figure 4.33. The difference in pressure between the inside and outside of the spherical drop can be calculated from a balance of forces on the sphere. The net force F arising from a pressure difference is

$$F = 4\pi r^2 P_{\rm in} - 4\pi r^2 P_{\rm ex} = 4\pi r^2 (P_{\rm in} - P_{\rm ex}), \tag{4.23}$$

where  $4\pi r^2$  is the surface area of the sphere, r is the radius,  $P_{\rm in}$  is the pressure inside the sphere and  $P_{\rm ex}$  is the pressure outside the sphere. This force must be balanced by the surface energy  $\gamma^{\rm LV}$  of the spherical surface. The work to enlarge the sphere by dr is F dr and must equal the surface work so that

$$F dr = \gamma^{LV} dA. \tag{4.24}$$

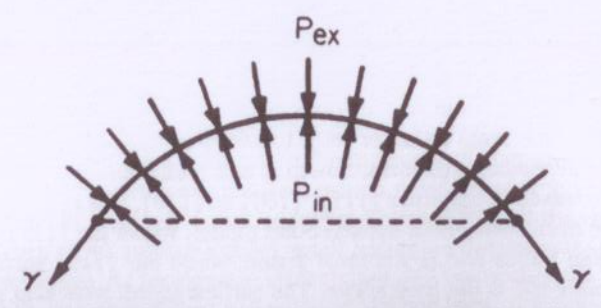


Figure 4.33. Section of a drop surface with internal pressure  $P_{\text{in}}$ , external pressure  $P_{\text{ex}}$ , radius r and surface energy  $\gamma$ . From [7].

Thus,

$$F = \gamma^{LV} \frac{\mathrm{d}A}{\mathrm{d}r} = 8\pi r \gamma^{LV} \tag{4.25}$$

and, from Eq. (4.23),

$$P_{\rm in} - P_{\rm ex} = \Delta P = 2\gamma^{\rm LV}/r. \tag{4.26}$$

Equation (4.26a) is sometimes referred to as LaPlace's equation. Since  $\gamma^{LV}$  is positive, the pressure inside a small drop or particle is always greater than it is outside. As an example, consider a drop of water 1  $\mu$ m in radius at room temperature, where  $\gamma^{LV} = 0.072 \text{ J/m}^2$ . From Eq. (4.26a),  $\Delta P = 1.44 \times 10^5 \text{ Pa}$  or approximately 1.4 atm. For a drop 0.01  $\mu$ m in radius, the pressure difference is 140 atm.

Now consider the case of a small single-component solid crystal in equilibrium with its vapor. For simplicity, we assume that the solid particle is spherical and has an isotropic surface stress f (Eq. 3.12). The surface stress exerts a hydrostatic pressure equal to 2f/r which is added to the pressure of the vapor to equal the pressure of the solid. Thus, the LaPlace pressure for the solid particle [2,3] can be expressed as

$$\Delta P = 2f/r. \tag{4.27a}$$

An equation very similar to Eq. (4.27a) can be derived for a cube of side length l. In this case, the surface area is  $6l^3$  and

$$\Delta P = 2f/l. \tag{4.27b}$$

Equation (4.27b) shows that the increased pressure inside a small crystal results from its size and not directly from its surface curvature. This principle applies to faceted crystals of any shape, although the situation is more complicated when different crystal facets have different surface energies. Of course, the curvature of a curved surface is related to its size. Thus, if a surface has two principal radii of curvature  $r_1$  and  $r_2$ , then

$$\Delta P = f(1/r_1 + 1/r_2),$$
 (4.27c)

where, for a sphere  $r_1 = r_2$  and for a long cylinder,  $r_2 = \infty$  and  $\Delta P = f/r$ .

Returning to the case of a liquid drop, since the Gibbs free energy contains a PV term, an increase in pressure P causes an increase in free energy G. From Eq. (3.13) at constant temperature and surface area

$$\Delta G = V \Delta P = 2 \gamma^{\text{LV}} V_{\text{m}} / r, \tag{4.28}$$

where  $V_{\rm m}$  is the molar volume of the phase. This free-energy increase from interfacial energy is often known as a capillarity effect or the Gibbs-Thompson effect. A similar expression including the surface stress can be written for solids [2,3].

Now let's consider how a particular physical property may vary with the size of a droplet. A simple case to treat is the vapor pressure of a drop with radius of curvature r. If we transfer atoms from the liquid droplet to the surrounding gas phase, there is a small and equal equilibrium displacement on both sides of the interface

$$dP_{in} - dP_{ex} = d(2\gamma^{LV}/r), \qquad (4.29)$$

where  $P_{\rm in}$  again refers to the droplet and  $P_{\rm ex}$  to the surrounding vapor. At constant temperature, the free-energy change associated with the transfer of atoms across the interface is given by

$$dG_{\rm in} = V_{\rm in} dP_{\rm in} \tag{4.30a}$$

and

$$dG_{\rm ex} = V_{\rm ex} dP_{\rm ex}.$$
 (4.30b)

At equilibrium, the free energy changes, are equal and we have

$$V_{\rm in} dP_{\rm in} = V_{\rm ex} dP_{\rm ex}. \tag{4.31}$$

Substituting Eq. (4.29) into Eq. (4.31) and rearranging yields

$$(V_{\rm ex} - V_{\rm in}) dP_{\rm ex}/V_{\rm in} = d(2\gamma^{\rm LV}/r).$$
 (4.32)

If we neglect the molar volume of the liquid with respect to the much larger molar volume of the gas and assume that the vapor behaves as an ideal gas, then

$$V_{\rm ex} = RT/P_{\rm ex} \tag{4.33}$$

and substituting this into Eq. (4.32) gives

$$dP_{ex}/P_{ex} = 2\gamma^{LV}V_{in}/RT d(1/r).$$
 (4.34)

We can now integrate Eq. (4.34) between the limits of a flat surface with zero curvature  $(1/r = 0, P = P_0)$  and some other state corresponding to a curved surface  $(1/r, P_{(r)})$  and assume that the molar volume of the liquid remains unchanged along this path. We obtain

$$ln(P_{(r)}/P_0) = 2\gamma^{LV}V_m/RTr, \qquad (4.35)$$

which is known as Kelvin's equation. It describes the dependence of the vapor pressure of any spherical particle on its size. From Eq. (4.35), we see that small particles have a higher vapor pressure than large particles. This feature has two important consequences:

- When there is a range of droplet sizes, the larger particles will grow at the expense of the smaller ones. This process is known as particle coarsening. Coarsening is important in many applications [67].
- 2. If a drop satisfying the above equation is in equilibrium with an infinite volume of vapor, this equilibrium is an unstable one. If the drop shrinks by evaporation then r decreases.  $P_{(r)}$  for equilibrium then increases above  $P_{(r)}$  existing in the vapor phase and the droplet evaporates completely. If the drop grows slightly by condensation then r increases. Now  $P_{(r)}$  for equilibrium is less than the existing  $P_{(r)}$  and the droplet tends to grow further. This concept of a droplet of given radius being in unstable equilibrium with a vapor at pressure  $P_{(r)} > P_0$  forms the basis of the capillarity theory of nucleation, a very important process.

An expression analogous to Eq. (4.35) has been derived for the change in solubility of a drop or particle in a two-phase system as a function of its size [2,3,68]. Small particles have greater solubility than large particles and the increased solubility can be quite substantial in the size range of 1–10 nm.

If we consider the effect of curvature on the equilibrium temperature of a liquid drop, we obtain the following equation,

$$\ln\left(T_{(r)}/T_0\right) = -(2\gamma^{LV}V_{in}/r\Delta H_v),\tag{4.36}$$

where T is the temperature, the subscripts have the same meaning as in Eq. (4.35) and  $\Delta H_{\rm v}$  is the molar heat of vaporization. This is known as the Thompson equation. If the pressure in the vapor phase is held constant, Eq. (4.36) shows that the small drops must be cooler to be in equilibrium with bulk liquid (note the minus sign). By comparison with Eq. 4.35, we see that at a given temperature, the drop has a higher vapor pressure. At a given pressure, the drop must be cooler to be in equilibrium with the bulk phase.

The effects mentioned above have particular relevance in current technology, where material structures and devices are being fabricated at the nanometer level [69] and surfaces contain a major fraction of the total number of atoms. To illustrate the magnitude of these effects, we discuss two cases involving the effect of particle size on the melting temperatures and lattice parameters of small gold crystals. The second topic encourages us to explore further the concept of surface stress introduced previously in Section 3.1. We conclude with a brief discussion of the stability of surfaces of stressed solids.

Figure 4.34 shows a graph of the melting temperature of small gold particles as a function of their size. The melting temperatures of the particles were determined by recording the temperature at which the crystalline spots in the electron diffraction patterns of the gold crystals disappeared when they were heated in the electron microscope. There is a dramatic decrease in  $T_{\rm m}$  (hundreds of degrees Kelvin) for particles less than 10 nm in size. The solid curve shown in Figure 4.34 was calculated according to the following equation,

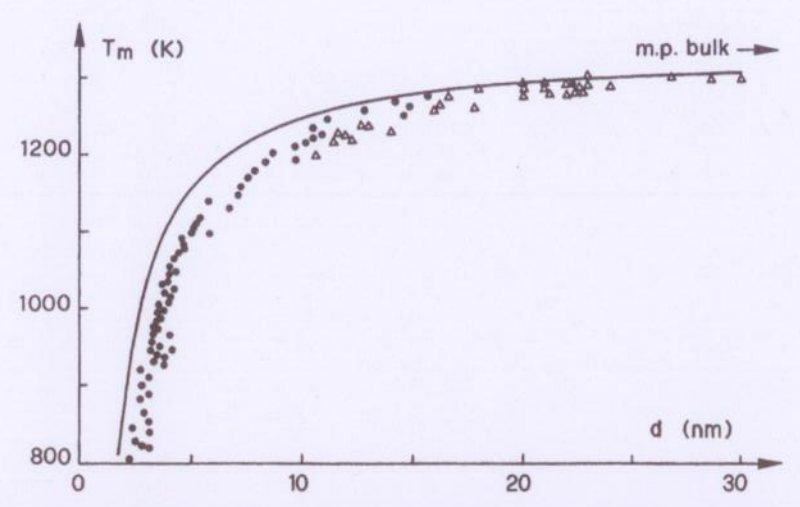


Figure 4.34. Melting temperature of small gold particles as a function of size. Reprinted from [71] with kind permission from Elsevier Science-NL, Amsterdam, The Netherlands.

$$\frac{T_{\rm m(r)}}{T_{\rm m(0)}} = 1 - 2V_{\rm m}^{\rm S}^{1/3} \left( \frac{\gamma^{\rm SV} V_{\rm m}^{\rm S}^{2/3} - \gamma^{\rm LV} V_{\rm m}^{\rm L}^{2/3}}{r \Delta H_{\rm s}} \right), \tag{4.37}$$

where  $T_{\rm m(r)}$  and  $T_{\rm m(0)}$  are the melting temperatures of the particle of radius r and bulk, respectively,  $V_{\rm m}^{\rm S}$  and  $V_{\rm m}^{\rm L}$  are the molar volumes of the solid and liquid, respectively,  $\gamma^{\rm SV}$  and  $\gamma^{\rm LV}$  are the surface free energies of the solid and liquid, respectively, and the other symbols have the same meanings as before [70]. This equation is similar to the Thompson equation (Eq. 4.36), but it includes contributions from the surface energies and molar volumes of both phases. It gives relatively good agreement with the experimental data except at the particle sizes where the effect is most pronounced. This difference has been attributed to the limitation of applying macroscopic thermodynamics developed for relatively large particles to atomic clusters. A microscopic approach has been developed that is able to more correctly account for the behavior of very small clusters [72]. We do not explore this approach here but instead look briefly at a few interesting properties of very small particles (nanocrystals).

So far, we have used macroscopic thermodynamic arguments to quantify the lowering of the melting temperature shown in Figure 4.34, but we can also rationalize this behavior using a nearest-neighbor bonding argument and considering the surface-to-volume ratio of very small clusters. For example, consider the two-dimensional close-packed clusters shown in Figure 4.35. The crystal on the left with radius  $r_1$  contains nineteen atoms, with twelve on the surface and seven in the interior. The crystal on the right with  $r_2 < r_1$  consists of seven atoms, with six on the surface and only one in the interior. As evident from Figure 4.35, the ratio of the number of surface atoms to interior atoms increases as the the particle size decreases; that is, the surface-to-volume ratio increases as the radius decreases. Because the

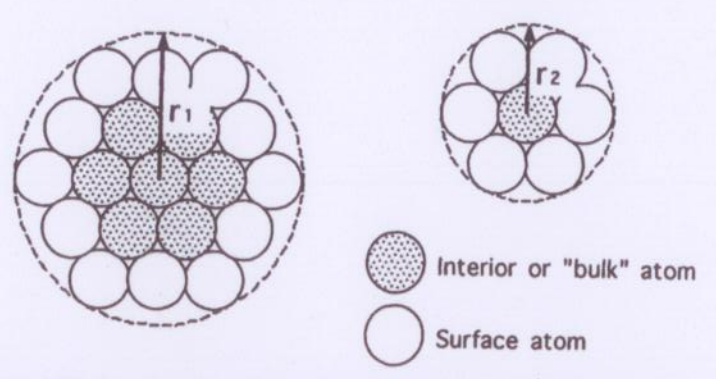


Figure 4.35. Two-dimensional illustration of two atomic clusters with radius  $r_2 < r_{1}$ .

surface atoms have more broken bonds than atoms in the interior (three versus six in this two-dimensional sketch), the free energy per unit volume of the particles increases as they become smaller. The small particle on the right has a higher free energy per unit volume (or atom) than the larger particle on the left. Hence, this particle is inherently less stable and will melt at a lower temperature than the large particle. In other words, on average it takes less energy per atom to separate the atoms in the small crystal compared to the large crystal, so the melting temperature is lower. In a complementary manner, we can also rationalize the melting of small particles at lower temperatures using the concept of surface melting discussed with reference to Figure 4.32.

The inherent instability of very small clusters because of their high surface area has been observed experimentally by HRTEM [73]. For example, Figure 4.36 shows a series of images of the same gold particle sitting on a SiO<sub>2</sub> substrate taken at 1/30-sec intervals. Examination of the atomic structure of the cluster shows that it is different in each image, varying from a cuboctahedra (Figs. 4.36c,e,f,k) to single twins (Fig. 4.36a,d,i) to multiply twinned particles (Figs. 4.36b,h,l). In this case, the energy of the electron beam is sufficient to cause the particle to rapidly fluctuate among a variety of structures, ranging from highly crystalline to almost liquidlike. This behavior has been called quasimelting [74] and is due to the high surface-to-volume ratio of the small crystals. Also notice the atomic terraces and ledges parallel to the close-packed {111} planes in images such as Figures 4.36a and c.

Another interesting dependence on particle size is shown in Figure 4.37. This figure shows the average lattice constant of small gold crystals as a function of their reciprocal radius [75]. What is particularly interesting about this study, is that the straight line in Figure 4.37, found by a least squares fit through the data, represents an interpretation of the experimental results in terms of the equation

$$f_{rr}^{SV} = -3r\Delta\alpha/2\vartheta\alpha, \tag{4.38}$$

where  $f_{rr}^{SV} = 1.175$  N/m is the surface stress in the radial direction (which is equal to  $\frac{1}{2}rP$ , where P is the hydrostatic pressure due to the sphere of radius r) when the

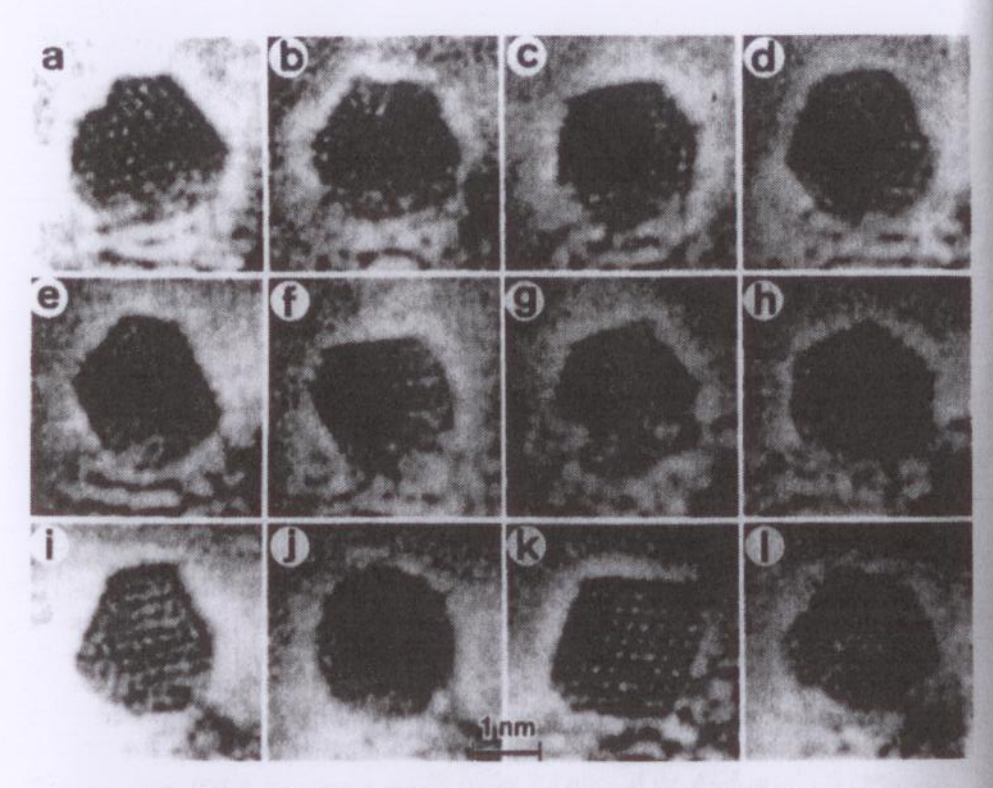


Figure 4.36. A series of HRTEM images showing various shapes of a gold cluster containing approximately 460 atoms. The images are single frames (1/30 sec) taken from a videocassette recording and the viewing direction is often along <110>. From [73].

bulk modulus for gold of  $\mathfrak{B}=5.99\times10^{-12}$  m<sup>2</sup>/N and lattice parameter  $\alpha=0.4080$  nm, appropriate to gold at 50°C are employed. The value  $\Delta\alpha$  is thus the change in lattice constant due to the surface stress. Since the specific surface free energy is by definition constant, the contraction of the lattice with decreasing particle size and hence the accompanying decrease in  $f_{\rm rr}$  is due to the surface stress.

When the value of 1400 mJ/m² was used for the bulk surface energy of gold, that is,  $G^s$  in the temperature range of 1017° to 1042°C, and an expression similar to Eq. (3.15) was used to extrapolate this value to 50°C, the experimental results were taken to indicate that the surface stress in the radial direction is negative with a numerical value of approximately 0.60 N/m. This is consistent with the discussion in Section 4.4 (Fig. 4.17), which indicated that atoms exposed to a surface should contract inward, generating a radial compressive stress in small particles. Hence, these experimental and theoretical analyses allow us to understand the influence of particle size on the surface stress. They also demonstrate that the magnitude of the surface stress can be significant in small particles where the number of atoms at the surface constitutes a large portion of the total number atoms in the particle.

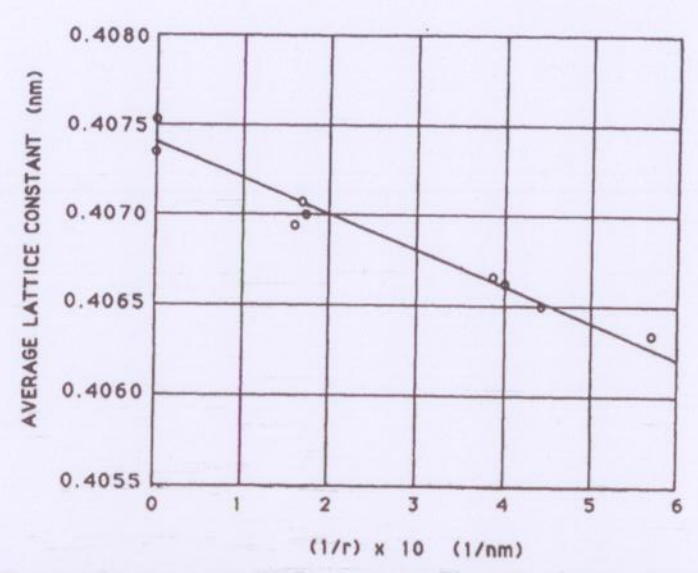


Figure 4.37. Average lattice constant of gold crystals as a function of their reciprocal radius. Reprinted from [75] with kind permission from Elsevier Science-NL, Amsterdam, The Netherlands.

In our discussions of surface relaxation and surface stress, we considered the contraction of atoms normal to the surface, and we envisioned the surface stress as acting tangentially along the surface, but we did not compare values for  $\gamma^{SV}$ ,  $f^{SV}$  or  $d\gamma^{SV}/de_{ij}$ . Table 4.5 shows values of the surface stress and surface energy for unreconstructed (111) and (100) surfaces of various f.c.c. metals calculated using EAM potentials [76]. In all cases, the surface stress is positive and generally higher for the less dense (100) surface than for the close-packed (111) surface. In the case of sil-

Table 4.5. Calculated surface free energy  $\gamma^{\rm sv}$  and principal surface stress  $f^{\rm sv}$  for clean, unreconstructed f.c.c. metal surfaces using EAM potentials

Sur	face	$\gamma^{SV}$ (J/m <sup>2</sup> )	f SV (J/m²)
Ni	(100)	1.57	1.27
	(111)	1.44	0.43
Cu	(100)	1.29	1.38
	(111)	1.18	0.86
Ag	(100)	0.70	0.82
	(111)	0.62	0.64
Au	(100)	0.92	1.79
	(111)	0.79	1.51
Pt	(100)	1.64	2.69
	(111)	1.44	2.86

Source: From [76].

ver,  $f^{\rm SV}$  and  $\gamma^{\rm SV}$  are similar in magnitude so that  ${\rm d}\gamma^{\rm SV}/{\rm d}e_{ij}$  is small, particularly for the (111) surface. In the case of nickel and copper,  $f^{\rm SV}$  is less than  $\gamma^{\rm SV}$  so that  ${\rm d}\gamma^{\rm SV}/{\rm d}e_{ij}$  is negative, wherease for gold and platinum,  $f^{\rm SV}$  is greater than  $\gamma^{\rm SV}$  so that  ${\rm d}\gamma^{\rm SV}/{\rm d}e_{ij}$  is positive. In both cases, the magnitude of  ${\rm d}\gamma^{\rm SV}/{\rm d}e_{ij}$  is often as large as either  $\gamma^{\rm SV}$  or  $f^{\rm SV}$ .

An interesting comparison of the specific surface free energies and surface stresses of the (111), (100) and (110) surfaces of a Lennard-Jones crystal as a function of temperature was performed using molecular dynamics by Broughton and Gilmer [77]. Some of their results are shown in Figure 4.38. The surface free energies  $\gamma^{SV}$  of the three crystal faces at low temperatures in Figure 4.38a are ordered exactly as expected from our earlier broken-bond model. The surface free energies decrease with temperature and become nearly equal (within the range of experimental error) for temperatures within about 10% of the melting temperature, as we expect from our previous analyses. In contrast to this behavior, the surface stresses f<sup>SV</sup> for the three crystal faces in Figure 4.38b are highly anisotropic, and this anisotropy persists up to  $T_{\rm m}$ . The stress in the (100) face is positive (tensile), whereas the stresses in the (111) and (110) faces are negative and approach a common value near  $T_m$ . The large compressive stress in the (111) face indicates that  $f^{SV}$  is negative and larger in magnitude that  $\gamma^{SV}$ . These results emphasize the anisotropic character of the surface stress and illustrate their importance, but it is difficult to obtain independent measurments of the surface stresses experimentally.

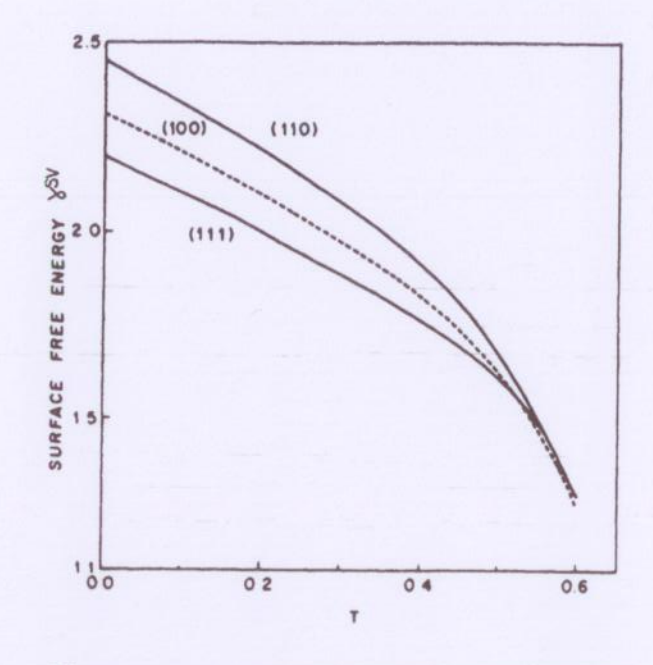
Before we leave the subject of surface stresses, we consider the issue of the morphological stability of a surface under stress. We only look at the end result of the analysis rather than to derive the results, since we will perform a more thorough development of the stability of a solid—liquid interface in the next part. At this time, we only show that solid surfaces may be unstable in the presence of a stress. This situation is particularly important in thin-film technology, where thin films on thick substrates are often left in a state of residual stress after fabrication, due to misfit (Eq. 4.21) and differential thermal contraction.

A simple energetic analysis can be used to illustrate the possible origin of a surface instability under an applied stress [78]. Consider the simple square-wave surface morphology shown in Figure 4.39, where the sample is stressed in the x direction. The change in energy in going from a flat surface to that shown in Figure 4.39 is roughly

$$\Delta E = (-\sigma^2/2Y)(c\lambda/2) + 2c\gamma^{SV}, \tag{4.39}$$

where  $\sigma$  is the stress in the bulk, c is the wave amplitude,  $\lambda$  is the wavelength,  $\gamma^{\rm SV}$  is the surface energy, Y is Young's modulus and it has been assumed that the stress is zero in the interior of the square protrusions. Equation (4.39) shows that the formation of this rough surface-profile lowers the energy of the system provided that the wavelength  $\lambda > 8\gamma^{\rm SV} Y/\sigma^2$ . Although this analysis is crude, it indicates why the surfaces of stressed bodies may be unstable.

A more rigorous kinetic stability analysis [78] demonstrates that initial flat surfaces bounding elastically stressed solids are unstable with respect to the formation



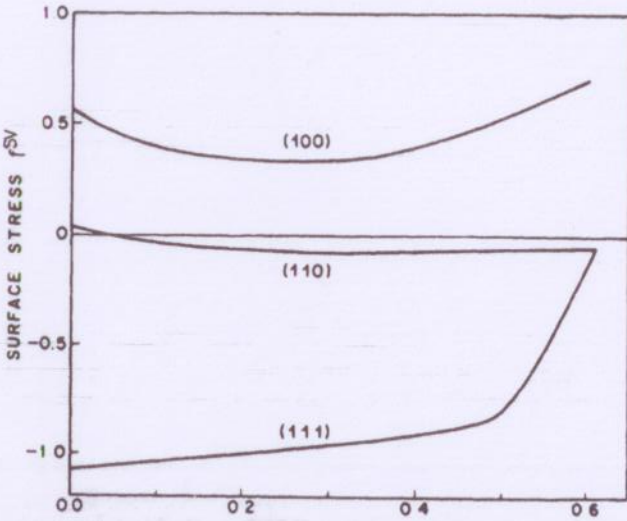


Figure 4.38. (a) The excess surface free energy versus temperature and (b) the surface stress versus temperature, for the (111), (100) and (110) surfaces of an LJ crystal. Tensile stresses are indicated by a positive sign in (b) and the melting temperature for the crystal  $T_{\rm m} = 0.617$  in the plots. Reprinted with permission from [77] by Elsevier Science Ltd., Oxford, England.

123

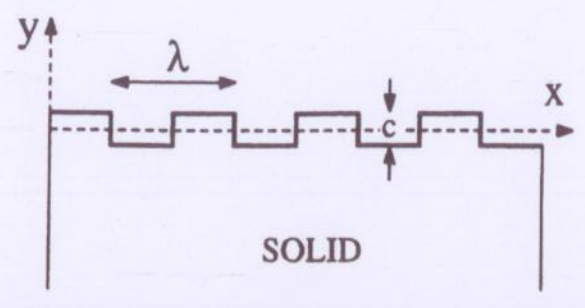


Figure 4.39. A solid with a square wave surface profile. The surface profile has wavelength \( \lambda \) and amplitude c/2. Reprinted with permission from [78] by Elsevier Science Ltd., Oxford, England.

of sinusoidal surface undulations (as opposed to a square wave profile) of wavelength greater than a critical wavelength  $\lambda_c$ . That wavelength and the maximally unstable wavelength  $\lambda_{max}$  were determined considering two reasonable types of matter transport on a surface; namely, surface diffusion, where mass transport occurs by atoms migrating across the surface, and evaporation-condensation, where atoms evaporate from the surface, migrate throught the vapor phase and condense at another location [79]. Although neither  $\lambda_c$  or  $\lambda_{max}$  depend on the magnitude of the transport coefficients, the rate at which perturbations of those wavelengths grow does. The results of these analyses are summarized in Figure 4.40. In the case of surface diffusion, a band of unstable sinusoidal modes exists with wavelengths \u03b1  $(=2\pi/k) > \lambda_c (=\pi Y \gamma^{SV}/\sigma^2)$  and with the most unstable mode at  $\lambda = \lambda_{max} = 4/3\lambda_c$ , where Y is the elastic modulus appropriate to the local surface orientation. These results imply that perturbations of wavelengths smaller than  $\lambda_c$  are smoothed by surface diffusion, whereas long wavelengths grow unstably. As it turns out, the value of

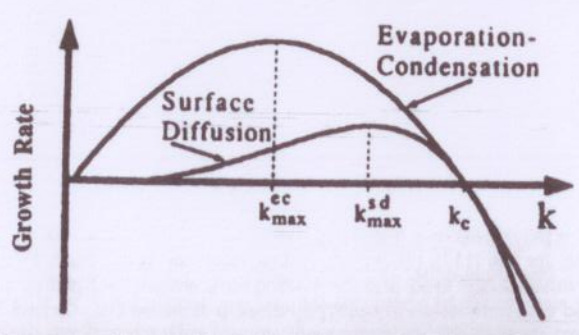


Figure 4.40. The exponential growth rate for surface perturbations of wavenumber  $k = 2\pi/\lambda$ ). The two curves are for surface diffusion (sd) and evaporation-condensation (ec) controlled growth. Perturbations with wavenumbers between 0 and kc are unstable, and the maximally unstable modes (\(\lambda\_{max}\)) are indicated for each growth process. Reprinted with permission from [78] by Elsevier Science Ltd., Oxford, England.

 $\lambda_{max}$  in the more rigorous analysis is within a factor of two of that given by  $\lambda$  in Eq. (4.39). In the case with evaporation-condensation as the transport mode, a similar band of unstable modes exists but with the most unstable mode at  $\lambda = \lambda_{max} = 2\lambda_{max}$ . Thus, although the smaller unstable wavelength is the same in both cases, the wavelength corresponding to the maximally unstable mode is 50% greater for the case of evaporation-condensation. These results demonstrate that surfaces of elastically stressed solids are unstable with respect to perturbations of wavelength greater than

$$\lambda_{\rm c} = \pi Y \gamma^{\rm SV} / \sigma^2. \tag{4.40}$$

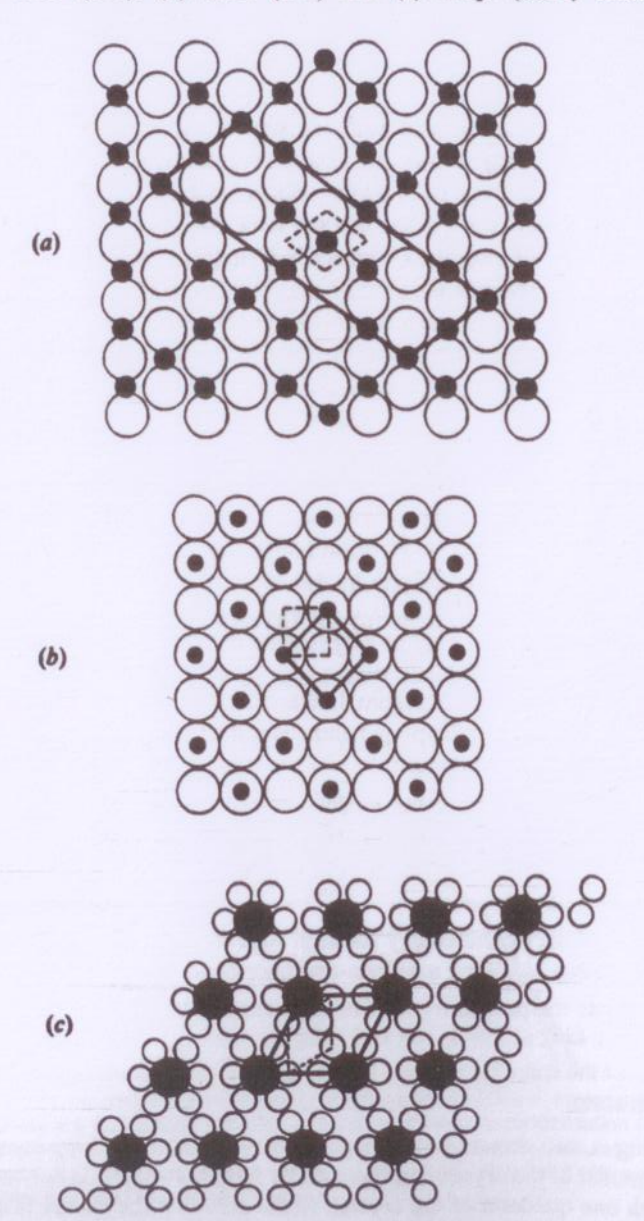
There are recent experimental data available for silicon-germanium alloy layers grown on silicon which suggest that this analysis is reasonable [80]. It has been included here to emphasize that a solid surface can be unstable in the presence of surface energies and stresses. We will see that the same concepts are applicable to solid-liquid and solid-solid interfaces, and there is ample experimental evidence to confirm the analysis in these cases.

#### **PROBLEMS**

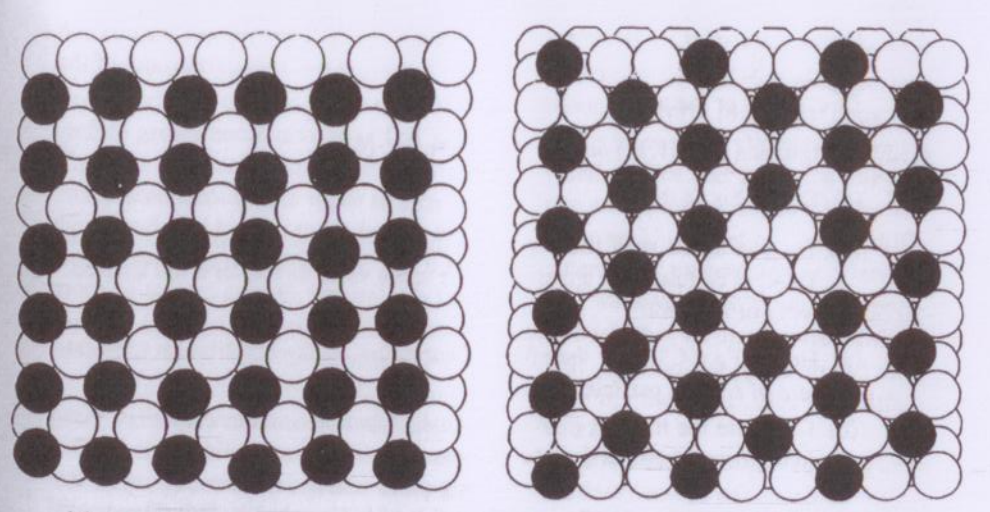
- 4.1. (a) Calculate the surface energies of the {111}, {100} and {110} planes of gold using the nearest-neighbor broken-bond model.
  - (b) Use Eq. (4.1) to plot the anisotropy of the surface energy for gold at 0 K from the low-energy {111} plane to the vicinal {332} plane. Explain the behavior of these results physically.
  - (c) How would your results in (a) and (b) differ if lead was used instead of gold?
- 4.2. (a) Use the data for lead in Figure 3.16 and Eqs. (4.2) to determine the value of  $E_{\rm l}$ , the excess enthalpy per unit length of ledge in Eq. (4.1), for the {100} and {111} surfaces.
  - (b) Calculate  $E_1$  for the same ledges, assuming a simple nearest-neighbor broken-bond model and compare your results with those in part (a).
- 4.3. Let the crystal in Figure 4.7 be a {111} f.c.c. silver surface with ledges that lie along a <110> direction.
  - (a) Calculate the excess energy for each state shown in Figure 4.7 relative to a kink atom assuming a nearest-neighbor bond model.
  - (b) Calculate the probability of finding a surface vacancy-adatom pair relative to a kink at T = 0, 100 and 1000 K.
  - (c) Repeat the same calculation for a ledge vacancy-adatom pair relative to a kink atom.
- 4.4. Assuming a two-dimensional simple-cubic crystal structure, construct an atomic model of the crystal in Figure 4.12a for  $0 < T < T_r$ . It is only necessary to sketch one quadrant of the crystal. Make sure that the corner is smoothly

rounded as shown in the figure. Does your model explain the deep cusp at  $\theta$  = 45° in Figure 4.12b?

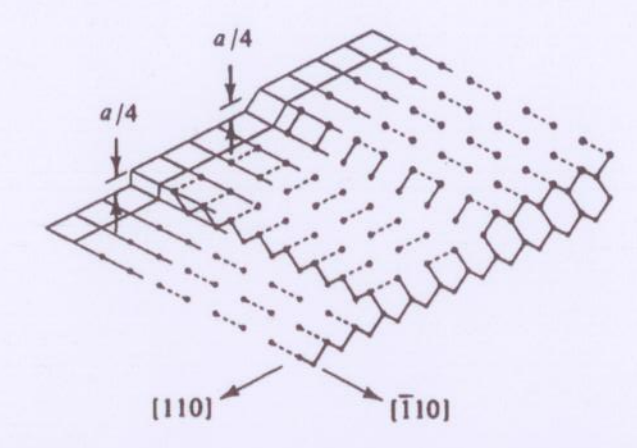
- 4.5. How would Eqs. (4.9a,b) differ if relaxation occurred around the vacancies or if there was a finite binding energy between the divacancies?
- 4.6. The three figures below show examples of commensurate surface layers on (a) b.c.c. (110), (b) f.c.c. (100) and (c) h.c.p. (0001) substrates (from



- [10]). The open and filled circles represent substrate and adsorbate atoms, respectively. The primitive translation vectors of both the substrate (dashed lines) and surface layer (solid lines) are also indicated.
- (a) Write the surface designation for each structure shown.
- (b) Find the adsorbate coverage for each of the three surfaces.
- 4.7. A {111} copper surface is initially covered with 19 adsorbed copper atoms per square centimeter. If it can be assumed that the bonding in the system can be described by the nearest-neighbor model:
  - (a) Calculate the change in energy per square centimeter if these adatoms accrete to form hexagonal islands of 19 atoms each.
  - (b) As the island size increases, how does the average number of bonds per atom change?
- 4.8. The two figures below (from [81]) show snapshots from Monte Carlo calculations of gold segregation to the: (a) {100} and (b) {111} surfaces of copper in a dilute copper—gold alloy. Use Figure 4.14 to determine the surface structure.



- 4.9. The figure on page 126 (from [53]) is a perspective view of a silicon (100) surface with single-layer high steps and terrace atom dimer orientation shifts on alternate layers.
  - (a) If a type A terrace is defined as one in which the atomic rows are parallel to the step edge and a type B terrace is one in which the atom rows are perpendicular to the step edge, identify the two terraces in the figure.
  - (b) Assuming that Figure 4.22b is a view normal to the terraces shown on page 126, show the orientation of the [110] direction in Figure 4.22b.
- 4.10. Use the atomic model of the gold (110) (1 × 2) reconstructed surface at the top of Figure 4.20 and a nearest-neighbor bond model to calculate the surface



energy of the reconstructed surface, assuming it is composed of {111} facets three atoms wide. Compare the resulting surface energy with that of an unreconstructed {110} surface determined by the nearest-neighbor bond model. Explain your results.

- 4.11. Given that the lattice parameter of graphite is 0.426 nm, calculate the misfit  $\delta$  of argon, krypton, and xenon on graphite, using the lattice parameters of the f.c.c. solids or the atomic radii of the elements.
- 4.12. Using Eqs. (1.8), (1.11) and (1.16), derive Eq. (4.22).
- 4.13. (a) Derive Eq. (4.26b).
  - (b) Do you agree with the statement that: "The vapor pressure of a small cube, in contrast to a sphere, has the same value as that of a flat surface." Why or why not?
- 4.14. (a) Derive Eq. (4.36) for the effect of curvature on the equilibrium temperature of a small particle.
  - (b) Calculate the melting point of a small, spherical indium crystal  $10^{-5}$  cm in diameter. Assume that the surface energies of both solid and liquid indium are 500 mJ/m<sup>2</sup> at the melting point and independent of crystallographic orientation. The melting point of indium is 156.6°C. The densities of the two phases are  $\rho^L = 7.02$  g/cm<sup>3</sup> and  $\rho^S = 7.31$  g/cm<sup>3</sup>, and the atomic weight is 114.8 amu. The heat of fusion is 6.07 kJ/mol.

# CRYSTAL GROWTH FROM THE VAPOR

In this chapter, we develop expressions that enable us to describe the growth rate of a solid-vapor interface under two limiting conditions. In one, we imagine that atoms arrive at the surface from the vapor and stick wherever they land. Thus, the surface grows continuously as fast as the atoms are transported through the vapor phase. In the second limiting case, we have a vicinal surface and the atoms must be transported through the vapor to a terrace, migrate across the terrace to a ledge and then attach at a kink in the ledge for the crystal to grow. This situation is more difficult to describe quantitatively, but it is a very interesting process and is often the mode of crystal growth. Hence, it is important that we develop quantitative expressions to describe this process. The concepts and models that we develop here can be compared with similar treatments that we will develop for solid-liquid and solid-solid interfaces in the following chapters, to see the similarities and differences in the growth behavior of these different interfaces.

We begin this section by first examining the situation where a surface grows uniformly as fast as atoms arrive at the surface. We then look at possible sources of ledges on a surface and include a brief discussion of nucleation theory. Having done this, we develop equations for the velocity of an individual ledge and a surface containing an array of ledges. We also treat the case of a continuous source of ledges, as found at a screw dislocation. We compare these different growth modes and then move on to a discussion of alloys in Chapter 6 and wetting between different phases in Chapter 7.

#### 5.1. CONTINUOUS GROWTH

The impingement rate or flux of atoms (or molecules) of a gas onto a solid surface exposed to the gas is given [33] by the expression